

# Polarized Anisotropic Stochastic Gravitational Wave Background Search with Ground-Based Detector Networks

Töre Boybeyi\* and Vuk Mandić†

*School of Physics and Astronomy, University of Minnesota, Minneapolis, MN 55455, USA*

(Dated: May 26, 2026)

Gravitational waves admit a Stokes decomposition into intensity ( $I$ ), circular polarization ( $V$ ), and linear polarization ( $Q, U$ ), analogous to Cosmic Microwave Background (CMB) polarimetry. We implement a full-Stokes maximum-likelihood SGWB map-making analysis for ground-based detector networks, promoting the standard cross-correlation data products used in existing pipelines to a joint reconstruction of  $I, V, Q, U$ . Applied to LVK O3 data, we constrain the polarized angular spectra  $C_\ell^{VV}, C_\ell^{EE}, C_\ell^{BB}$  and  $|C_\ell^{IV}|$ . We show that an intensity-only model is biased when polarized sky components are present, since the detector-network Fisher inner product does not generally make the Stokes responses orthogonal. For transient CBC foregrounds, polarized shot noise is not parametrically suppressed relative to ordinary CBC intensity shot noise. The full Stokes framework separates the Stokes sectors while providing access to polarized anisotropies invisible to conventional intensity-only searches.

*Introduction.* The direct observation of gravitational waves (GWs) has opened a new window on the Universe, with hundreds of compact binary coalescence (CBC) candidates detected by the LIGO/Virgo/KAGRA (LVK) collaboration [1–4] and evidence for a stochastic gravitational wave background (SGWB) at nanohertz frequencies emerging from pulsar timing arrays [5–9]. As sensitivity improves, characterizing the SGWB beyond its spectrum to include angular anisotropies and polarization becomes both feasible and scientifically compelling [10–22]. Because the SGWB is sourced by both astrophysical populations and possible primordial relics, its spectrum, anisotropy, and polarization encode information about compact binary demographics and large scale structure, as well as early Universe dynamics such as phase transitions or inflation [23–29].

Just as the cosmic microwave background (CMB) is fully characterized by its Stokes parameters  $\{I, Q, U, V\}$ , the SGWB possesses an analogous polarization structure encoding qualitatively new information [14–16, 30, 31]. The intensity anisotropy traces the spatial distribution of GW sources and large scale structure [11, 12], circular polarization ( $V$ ) probes parity violation in the gravitational sector [14, 15, 32], and linear polarization ( $Q, U$ ) constrains the orbital geometry of the source population. Existing anisotropic ground-based SGWB map-making searches have reconstructed only the intensity channel [33–37], leaving the polarized Stokes fields unmodeled.

In this *Letter*, we introduce a full Stokes SGWB search framework for ground-based networks that jointly reconstructs  $I, V, Q, U$  from the standard cross-correlation data. We apply it to LVK O3 data, constraining  $C_\ell^{VV}, C_\ell^{EE}, C_\ell^{BB}$ , and  $|C_\ell^{IV}|$ . We validate the framework through simulations and demonstrate how unmodeled polarization can leak into intensity-only anisotropy estimates.

*Formalism.* We work in the frequency domain and ex-

pand the GW strain arriving from sky direction  $\hat{\Omega}$  in terms of the tensor polarization basis  $e_{ij}^{(s)}(\hat{\Omega})$  (see Supplemental Material (SM) S-I):

$$\tilde{h}_{ij}(f, \hat{\Omega}) = \sum_{s \in \{\pm 2\}} e_{ij}^{(s)}(\hat{\Omega}) \tilde{h}^{(s)}(f, \hat{\Omega}), \quad (1)$$

where the sum is restricted to the two tensor helicities  $s = \pm 2$ ; vector and scalar modes, which have been targeted in separate stochastic-polarization searches [13], are set to zero throughout. We expand the two-point strain correlation function as:

$$\langle \tilde{h}^{(s_1)}(f_1, \hat{\Omega}_1) \tilde{h}^{*(s_2)}(f_2, \hat{\Omega}_2) \rangle = \frac{1}{2} \delta(f_1 - f_2) \delta^{(2)}(\hat{\Omega}_1 - \hat{\Omega}_2) \mathcal{H}_{s_1 s_2}(f_1; \hat{\Omega}_1), \quad (2)$$

where  $\mathcal{H}$  contains the standard gravitational Stokes parameters [19]:

$$\mathcal{H}_{s_1 s_2}(f, \hat{\Omega}) = \frac{1}{2} \begin{pmatrix} I + V & P^- \\ P^+ & I - V \end{pmatrix} (f, \hat{\Omega}). \quad (3)$$

and we assumed different directions to be uncorrelated. The rows are labeled by  $s_1 \in \{+2, -2\}$  and the columns by  $s_2 \in \{+2, -2\}$ . The linear polarization fields  $P^\pm \equiv Q \pm iU$  transform as  $P^\pm \rightarrow e^{\mp 4i\psi} P^\pm$  under a local basis rotation by  $\psi$ , identifying them as spin- $\pm 4$  fields (spin-4 arising from the product of two spin-2 tensors), whereas  $I$  and  $V$  are spin-0. When expanded in spin-weighted spherical harmonics  ${}_{\pm 4}Y_{\ell m}$ , the linear polarization coefficients  $a_{\ell m}^\pm$  separate into parity-even (gradient,  $E$ ) and parity-odd (curl,  $B$ ) components,  $a_{\ell m}^E = -(a_{\ell m}^+ + a_{\ell m}^-)/2$  and  $a_{\ell m}^B = i(a_{\ell m}^+ - a_{\ell m}^-)/2$ , in direct analogy with CMB polarimetry [31, 38]. Since spin- $\pm 4$  harmonics exist only for  $\ell \geq 4$ , the  $E$  and  $B$  spectra also begin at  $\ell = 4$ .

We consider a detector  $\mathcal{I}$  at position  $\vec{x}_{\mathcal{I}}$ , whose output  $\tilde{s}_{\mathcal{I}}(f; t)$  during a time-segment labeled by  $t$  combines instrumental noise  $\tilde{n}_{\mathcal{I}}(f; t)$  with the sky integrated

projection of the GW strain onto the detector geometry [19]. For each baseline  $\mathcal{IJ}$  and Stokes parameter  $X \in \{I, V, P^\pm\}$ , one defines direction dependent overlap reduction functions (ORFs)  $\Gamma_{\mathcal{IJ}}^X(f, \hat{\Omega}; t)$  built from the antenna patterns  $F_{\mathcal{I}}^{+, \times}$  and the baseline phase factor [39–41] (explicit forms in SM).

We compute the one sided cross spectrum  $\hat{C}_{\mathcal{IJ}}(f; t) \equiv \frac{1}{\tau} \tilde{s}_{\mathcal{I}}(f; t) \tilde{s}_{\mathcal{J}}^*(f; t)$  from short Fourier segments of duration  $\tau$ . We define the  $\Omega$ -normalized Stokes fields  $\Omega_X(f, \hat{\Omega}) \equiv \frac{2\pi^2 f^3}{3H_0^2} X(f, \hat{\Omega})$  for  $X \in \{I, V, Q, U\}$ . Assuming a power-law spectrum  $\Omega_X(f, \hat{\Omega}) = H(f) \Omega_X(\hat{\Omega})$  with  $H(f) = (f/f_{\text{ref}})^\alpha$ , we expand the angular dependence in a spatial basis indexed by  $\kappa$  (where  $\kappa = \ell m$  in the spherical harmonic (SH) basis or a pixel index  $p$  in a pixel basis):

$$\Omega_X(\hat{\Omega}) = \sum_{\kappa} \Omega_{\kappa}^X \Psi_{\kappa}^X(\hat{\Omega}). \quad (4)$$

Following the standard radiometer and maximum-likelihood SGWB map-making formalism [33–35, 42], the estimator for the (clean map) anisotropy coefficients is  $\hat{\Omega} = \mathcal{F}^{-1} \hat{\mathcal{X}}$ , with

$$\mathcal{F}_{\kappa\kappa'}^{XY} = \sum_{\substack{\mathcal{I} < \mathcal{J} \\ f, t}} \frac{[\tilde{\Gamma}_{\mathcal{IJ}; \kappa}^X]^* \tilde{\Gamma}_{\mathcal{IJ}; \kappa'}^Y}{\bar{P}_{\mathcal{I}}(f, t) \bar{P}_{\mathcal{J}}(f, t)}, \quad (5)$$

$$\hat{\mathcal{X}}_{\kappa}^X = \sum_{\substack{\mathcal{I} < \mathcal{J} \\ f, t}} \frac{[\tilde{\Gamma}_{\mathcal{IJ}; \kappa}^X]^* \hat{C}_{\mathcal{IJ}}(f; t)}{\bar{P}_{\mathcal{I}}(f, t) \bar{P}_{\mathcal{J}}(f, t)}, \quad (6)$$

where  $\bar{P}_{\mathcal{I}}(f, t)$  are the estimated noise power spectral densities (PSDs),  $\tilde{\Gamma}_{\mathcal{IJ}; \kappa}^X(f, t) \equiv \frac{3H_0^2}{4\pi^2 f^3} H(f) \int d\hat{\Omega} \Gamma_{\mathcal{IJ}}^X(f, \hat{\Omega}; t) \Psi_{\kappa}^X(\hat{\Omega})$  are the  $\Omega$ -normalized responses projected onto the spatial basis, and the sums run over all baselines, frequency bins, and time segments. The Fisher matrices  $\mathcal{F}$  can be ill-conditioned and, when needed, we use a regularized pseudoinverse with poorly measured eigenmodes removed.

A key consequence of the joint Stokes treatment is the identification of a systematic bias in the standard intensity-only analysis. Because the dirty map  $\hat{\mathcal{X}}^I$  receives contributions from all Stokes parameters, the  $I$  only clean map  $\hat{\Omega}_{\kappa}^I = \sum_{\kappa'} (\mathcal{F}_{II})_{\kappa\kappa'}^{-1} \hat{\mathcal{X}}_{\kappa'}^I$  cannot distinguish polarization from intensity. The Stokes fields are physically distinct, but their detector responses are not generally orthogonal under the network Fisher inner product. Its expectation is

$$\langle \hat{\Omega}_{\kappa}^I \rangle = \Omega_{\kappa}^I + \sum_{\beta, \kappa'} \Omega_{\kappa'}^{\beta} \underbrace{\sum_{\kappa''} (\mathcal{F}_{II})_{\kappa\kappa''}^{-1} \mathcal{F}_{\kappa''\kappa'}^{I\beta}}_{\mathcal{L}_{\kappa\kappa'}^{\beta}}, \quad (7)$$

where  $\beta \in \{V, +, -\}$  and  $\mathcal{L}^{\beta}$  is the leakage matrix. For persistent sources  $\Omega_{\kappa'}^{\beta}$  is fixed, so the bias does not aver-

age away with longer observation. An exact full block inversion removes this modeled leakage at the cost of larger marginalized intensity uncertainties.

*Validation.* We simulate a persistent, polarized sky observed by the LIGO Hanford, LIGO Livingston, and Virgo (HLV) network at expected O5 sensitivity [43] with three years of stationary Gaussian noise. The simulation consists of an unpolarized galactic plane with amplitude  $10^{-6} (f/25 \text{ Hz})^{-7/3}$ , a circularly polarized cap with polarization degree  $p = 0.8$  (pure  $V$ ), and a linearly polarized cap ( $p = 0.8$ , mixed  $Q/U$ ), where  $p \equiv \sqrt{Q^2 + U^2 + V^2}/I$  quantifies the fractional polarization; see SM Sec. S-II A for the full parameterization. We reconstruct the sky in both the SH basis (up to maximum multipole  $\ell_{\text{max}} = 24$ ) and the pixel basis (HEALPIX [44],  $N_{\text{side}} = 8$ , corresponding to 768 pixels).

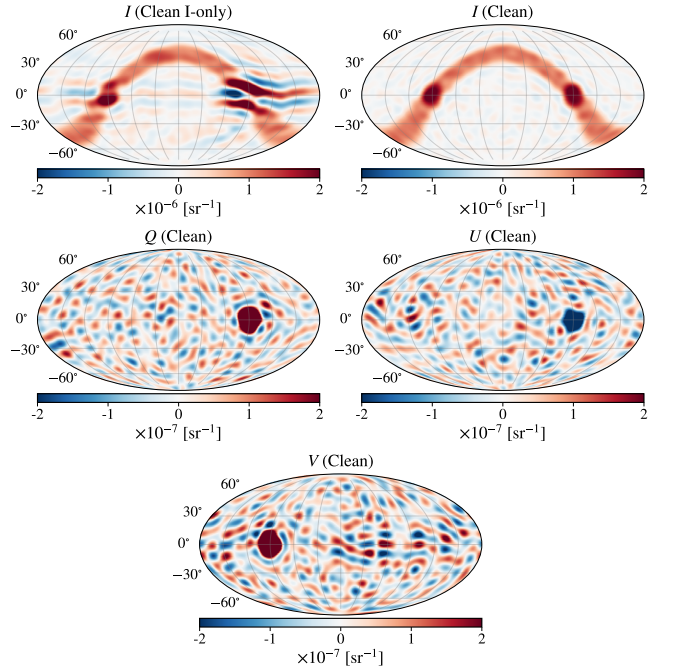


FIG. 1. Recovered clean maps in the spherical harmonic basis for the benchmark simulation. Top row compares the  $I$  only (left) and full Stokes (right) intensity reconstructions; the  $I$  only map shows visible contamination from unmodeled polarization. Bottom row shows the full Stokes  $V$ ,  $Q$ , and  $U$  clean maps, recovering the simulated circularly and linearly polarized caps. Color bars indicate  $\Omega_X$  in units of  $\text{sr}^{-1}$ .

The full Stokes reconstruction recovers the simulated morphology in all Stokes sectors in both bases, with per pixel SNR  $\sim \mathcal{O}(10)$  for the unpolarized plane and SNR  $\sim \mathcal{O}(1-10)$  for the polarized caps, as shown in Fig. 1. The normalized residual maps, presented in SM Sec. S-II A, are consistent with Gaussian noise, showing no detectable reconstruction bias in the retained modes. Repeating the analysis with the  $I$  only pipeline, the recovered intensity clean map shows visible contamina-

tion from the unmodeled polarization (Fig. 1, top left); the corresponding normalized residuals exceed  $10\sigma$  (SM Fig. S4), directly visualizing the polarization leakage of Eq. (7).

*Case study.* In addition to biasing the intensity map (Eq. (7) and Fig. 1), neglecting polarization leads to incorrect estimation of the angular power spectrum. Forming  $\hat{C}_\ell^{II} = (2\ell+1)^{-1} \sum_m |\hat{a}_{\ell m}^I|^2$  from the  $I$ -only clean map and averaging over source realizations gives  $\langle \hat{C}_\ell^{II} \rangle = C_\ell^{II} + \Delta C_\ell^{\text{pol}} + \Delta C_\ell^{\text{noise}}$ , where  $\Delta C_\ell^{\text{noise}}$  is the detector noise bias [45]. The polarized term is generated by the projection of unmodeled Stokes components through the leakage matrix in Eq. (7). For transient CBC foregrounds this contribution has the same observing-time scaling as the ordinary CBC shot noise [45–47], but it is not parametrically suppressed relative to it.

For compact binaries with isotropically distributed inclinations, the ratio of the circular-polarization shot-noise power to the intensity shot-noise power is  $C_\ell^{VV, \text{shot}}/C_\ell^{II, \text{shot}} = \langle g_V^2 \rangle / \langle g_I^2 \rangle \approx 0.97$ , where  $g_I = (1 + \cos^2 \iota)^2/4 + \cos^2 \iota$  and  $g_V = \cos \iota (1 + \cos^2 \iota)$  are inclination-dependent responses (SM Sec. S-V). Thus polarized shot-noise leakage can be comparable to the conventional CBC intensity shot-noise floor, with the actual size set by detector geometry and the leakage matrix.

We demonstrate these effects for a third-generation network consisting of one 40 km Cosmic Explorer (CE) at the current LIGO Hanford site [48] and a two-detector Einstein Telescope in the 2L configuration [49], with the two 15 km L-shaped interferometers located at Sos Enattos (Sardinia) and the Meuse Rhine Euroregion (Netherlands/Belgium/Germany). We simulate three years of observation and model the astrophysical foreground using a simplified CBC population calibrated to GWTC-4 rates [25] (SM Sec. S-V), with events above a network SNR  $> 20$  individually resolved and subtracted. The residual population produces a polarized shot-noise foreground, consistent with the circular polarization generated by Poisson fluctuations of unresolved binaries [47, 50], which through Eq. (7) contaminates the intensity-only estimator and pushes  $\langle \hat{C}_\ell^{II} \rangle$  above the true  $C_\ell^{II}$ , as shown in Fig. 2. On top of this foreground we simulate a circularly polarized cosmic monopole at  $\alpha = 0$  with  $\Pi_V \equiv \Omega_V^{\text{cos}}/\Omega_T^{\text{cos}} = 0.1$ , the circular polarization fraction of the cosmic component, representative of a primordial chiral signal [51]. The simulated  $V$  monopole amplitude is near the CBC shot-noise level, making it challenging for a standard isotropic parity violation search [14, 15]. Meanwhile the conventional  $I$ -only anisotropic analysis is structurally blind to polarization: it merely adds the cosmic intensity into the overall monopole, while the polarized shot noise biases  $\hat{C}_\ell^{II}$  upward through Eq. (S61). For this case study we restrict to the low multipoles shown in Fig. 2; the Fisher matrix is well conditioned, so no eigenmode truncation is

applied.

Fig. 2 illustrates how the full-Stokes analysis changes the picture in two ways. First, the full block inversion removes the polarization leakage from the recovered intensity spectrum, leaving the residual  $\ell > 0$  power consistent with the expected shot-noise fluctuations. Second, it reconstructs the  $I$ - $V$  cross spectrum  $C_0^{IV}$ , giving direct access to parity-odd intensity-circular correlations. The cost of the full-Stokes analysis is a modest increase in intensity noise: from the Schur complement of the block Fisher matrix (SM Sec. S-III), the detector-noise contribution to the monopole variance is approximately 1.4 times larger in the full-Stokes analysis; however, the  $I$ -only estimator incurs additional realization-dependent variance from the polarization leakage, so the total scatter of the two analyses is comparable at  $\ell \geq 1$  (Fig. 2). We note that the full-Stokes framework fits  $I$  and  $V$  as independent parameter blocks and accesses their cross spectrum, providing a direct handle on the polarization fraction  $\Pi_V$ .

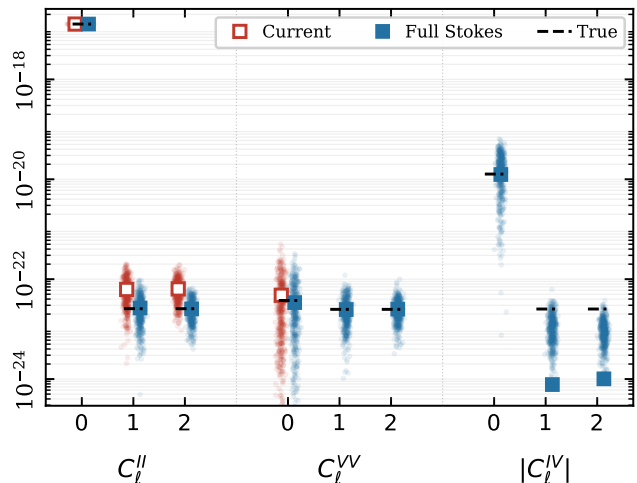


FIG. 2. Angular power spectra for a CE+ET(2L) network with a simulated CBC foreground and a circularly polarized cosmic monopole ( $\Pi_V = 0.1$ ,  $\alpha = 0$ ). Open (filled) markers show the  $I$ -only (full-Stokes) analysis. Dashes mark the expected signal plus shot-noise level; dots show individual Monte Carlo realizations. See text for details.

*O3 results.* We apply the full Stokes formalism to the publicly available folded cross-correlation data from the first three observing runs of Advanced LIGO and Advanced Virgo [10, 37], the most recent dataset for which the required baseline cross-spectra are publicly released [52]. Pixel basis upper limit maps are reported as GW energy flux density  $F_\alpha$  (SM Eq. (S29)); angular power spectra are reported as  $\Omega$ . We combine the HL baseline from O1, O2, and O3, together with the HV and LV baselines from O3. In the pixel basis ( $N_{\text{side}} = 16$ , corresponding to 3072 pixels) we produce sky maps for spectral indices  $\alpha \in \{0, 2/3, 3\}$ ; in the spherical har-

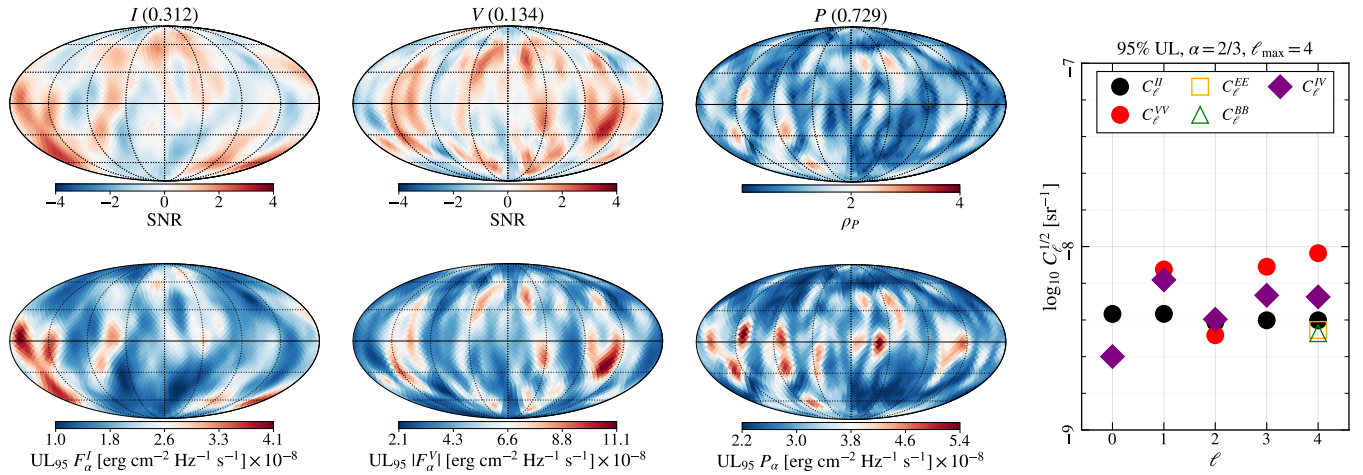


FIG. 3. Results from the full-Stokes analysis of the LVK O3 data at  $\alpha = 2/3$ . The first three columns show the SNR (top) and the 95% confidence level upper limit (bottom) maps for Intensity ( $I$ ), Circular Polarization ( $V$ ), and total Linear Polarization amplitude ( $P \equiv \sqrt{Q^2 + U^2}$ ), respectively. Numbers in parentheses in the map titles give the corresponding global  $p$ -values (SM Sec. S-IV). The fourth panel displays the corresponding 95% bounds on the angular spectra. For the parity-odd cross spectrum, we plot the 95% bound  $|C_\ell^{IV}|_{95}^{1/2}$ . Since  $E$  and  $B$  begin at  $\ell = 4$ , the O3 linear-polarization power constraints correspond only to  $\ell = 4$ .

monic basis we analyze up to  $\ell_{\max} = 4$  at  $\alpha = 2/3$ , following the pixel and spherical-harmonic map-making approaches used in analyses [37, 42, 53]. Since  $E$  and  $B$  begin at  $\ell = 4$ , this O3 analysis constrains only the  $\ell = 4$  linear-polarization power. From the clean maps we estimate the angular power spectra [35]

$$\hat{C}_\ell^{XY} = \frac{1}{2\ell + 1} \sum_m \text{Re}[\hat{\Omega}_{\ell m}^X \hat{\Omega}_{\ell m}^{Y*}] - N_\ell^{XY}, \quad (8)$$

where  $N_\ell^{XY} = (2\ell + 1)^{-1} \sum_m \text{Re}[(\mathcal{F}^{-1})_{\ell m, \ell m}^{XY}]$  is the corresponding noise bias.

The results at  $\alpha = 2/3$  are summarized in Fig. 3 (see SM Fig. S7 for  $\alpha = 0$  and  $\alpha = 3$ ). We find no significant anisotropy in any Stokes parameter. Each map is characterized by the per-pixel radiometer SNR map,  $\hat{X}_{\hat{n}}/\sqrt{\Gamma_{\hat{n}\hat{n}}}$  [35, 37]; for linear polarization we use the statistic  $\rho_P^2(p) = (\hat{\Omega}_p^Q, \hat{\Omega}_p^U) [(\mathcal{F}^{-1})_{pp}^{XY}]_{X,Y=Q,U}^{-1} (\hat{\Omega}_p^Q, \hat{\Omega}_p^U)^T$  that is invariant under polarization basis rotation. The global significance is assessed from a noise-only Monte Carlo that preserves the sky covariance, detailed in SM Sec. S-IV A. At  $\alpha = 2/3$  the maximum per-pixel values are SNR  $\simeq 2.9$  for  $I$ , 3.2 for  $V$  and  $\rho_P \simeq 2.8$ , with global  $p$ -values 0.31, 0.13 and 0.73; the corresponding null distributions are shown in SM Fig. S8. The first three columns of Fig. 3 show the SNR and the 95% upper-limit maps for  $I$ ,  $V$  and the total linear-polarization amplitude  $P \equiv \sqrt{Q^2 + U^2}$ . The fourth panel presents the 95% bounds on the angular spectra, with the calibration-marginalized Bayesian posterior of Ref. [54]. Marginalizing over the polarized Stokes parameters broadens the intensity bound: the joint  $C_\ell^{II/2}$  upper limits sit roughly a factor of 2 above

an  $I$ -only analysis, the median ratio being about 2.2, 2.5 and 3.0 at  $\alpha = 0, 2/3$  and 3. The  $C_\ell^{VV}$ ,  $C_\ell^{EE}$ ,  $C_\ell^{BB}$  and  $|C_\ell^{IV}|$  bounds are obtained from a joint full-Stokes ground-based analysis.

The parity-odd cross-spectrum  $C_\ell^{IV}$  is of particular interest as a probe of gravitational parity violation. For an isotropically oriented CBC population, the inclination-averaged cross-response vanishes ( $\langle g_I g_V \rangle = 0$ ; SM Sec. S-V), so the ensemble-mean CBC shot-noise bias in  $C_\ell^{IV}$  vanishes. Finite realizations still contribute variance, but not a positive semidefinite systematic bias analogous to  $C_\ell^{VV}$ . Thus  $C_\ell^{IV}$  provides a useful parity-odd observable for constraining mechanisms such as Chern-Simons gravity [51], chiral gravitational-wave production in the early Universe [14, 15], and parity-violating propagation searched for or constrained with SGWB data [55, 56].

*Conclusion.* We have implemented a full Stokes SGWB search framework that jointly reconstructs  $I, V, Q, U$  from existing ground-based cross-correlation data. Applied to LVK O3 data, we find no significant polarization anisotropy and place bounds on  $C_\ell^{VV}$ ,  $C_\ell^{EE}$ ,  $C_\ell^{BB}$ , and  $|C_\ell^{IV}|$ . Simulations for future detector networks demonstrate that neglecting polarization can bias intensity-only anisotropy estimates through polarized sky components and CBC shot-noise leakage. The full Stokes framework separates the Stokes sectors and provides access to polarized anisotropies invisible to conventional intensity-only searches.

*Acknowledgments:* We are grateful to Deepali Agarwal and the LVK Stochastic Group for valuable comments and feedback on the draft. TB and VM were in part supported by the NSF grant PHY-2409173.

This research has made use of data or software obtained from the Gravitational Wave Open Science Center (gwosc.org), a service of the LIGO Scientific Collaboration, the Virgo Collaboration, and KAGRA. This material is based upon work supported by LIGO Laboratory which is a major facility fully funded by the National Science Foundation, as well as the Science and Technology Facilities Council (STFC) of the United Kingdom, the Max-Planck-Society (MPS), and the State of Niedersachsen/Germany for support of the construction of Advanced LIGO and construction and operation of the GEO600 detector. Additional support for Advanced LIGO was provided by the Australian Research Council. Virgo is funded, through the European Gravitational Observatory (EGO), by the French Centre National de Recherche Scientifique (CNRS), the Italian Istituto Nazionale di Fisica Nucleare (INFN) and the Dutch Nikhef, with contributions by institutions from Belgium, Germany, Greece, Hungary, Ireland, Japan, Monaco, Poland, Portugal, Spain. KAGRA is supported by Ministry of Education, Culture, Sports, Science and Technology (MEXT), Japan Society for the Promotion of Science (JSPS) in Japan; National Research Foundation (NRF) and Ministry of Science and ICT (MSIT) in Korea; Academia Sinica (AS) and National Science and Technology Council (NSTC) in Taiwan.

---

\* boybe001@umn.edu

† vuk@umn.edu

- [1] A. G. Abac *et al.* (LIGO Scientific, VIRGO, KAGRA), GWTC-4.0: Updating the Gravitational-Wave Transient Catalog with Observations from the First Part of the Fourth LIGO-Virgo-KAGRA Observing Run, arXiv e-prints (2025), arXiv:2508.18082 [gr-qc].
- [2] R. Abbott *et al.* (KAGRA, VIRGO, LIGO Scientific), GWTC-3: Compact Binary Coalescences Observed by LIGO and Virgo during the Second Part of the Third Observing Run, Phys. Rev. X **13**, 041039 (2023), arXiv:2111.03606 [gr-qc].
- [3] B. P. Abbott *et al.* (LIGO Scientific, Virgo), Observation of Gravitational Waves from a Binary Black Hole Merger, Phys. Rev. Lett. **116**, 061102 (2016), arXiv:1602.03837 [gr-qc].
- [4] B. P. Abbott *et al.* (LIGO Scientific, Virgo), GW170817: Observation of Gravitational Waves from a Binary Neutron Star Inspiral, Phys. Rev. Lett. **119**, 161101 (2017), arXiv:1710.05832 [gr-qc].
- [5] G. Agazie *et al.* (NANOGrav), The NANOGrav 15 yr Data Set: Evidence for a Gravitational-wave Background, Astrophys. J. Lett. **951**, L8 (2023), arXiv:2306.16213 [astro-ph.HE].
- [6] Z. Arzoumanian *et al.* (NANOGrav), The NANOGrav 12.5 yr Data Set: Search for an Isotropic Stochastic Gravitational-wave Background, Astrophys. J. Lett. **905**, L34 (2020), arXiv:2009.04496 [astro-ph.HE].
- [7] J. Antoniadis *et al.* (EPTA, InPTA:), The second data release from the European Pulsar Timing Array - III. Search for gravitational wave signals, Astron. Astrophys. **678**, A50 (2023), arXiv:2306.16214 [astro-ph.HE].
- [8] D. J. Reardon, A. Zic, R. M. Shannon, G. B. Hobbs, M. Bailes, V. Di Marco, A. Kapur, A. F. Rogers, E. Thrane, J. Askew, *et al.*, Search for an isotropic gravitational-wave background with the parkes pulsar timing array, The Astrophysical Journal Letters **951**, L6 (2023).
- [9] H. Xu *et al.*, Searching for the Nano-Hertz Stochastic Gravitational Wave Background with the Chinese Pulsar Timing Array Data Release I, Res. Astron. Astrophys. **23**, 075024 (2023), arXiv:2306.16216 [astro-ph.HE].
- [10] R. Abbott *et al.* (KAGRA, Virgo, LIGO Scientific), Upper limits on the isotropic gravitational-wave background from Advanced LIGO and Advanced Virgo's third observing run, Phys. Rev. D **104**, 022004 (2021), arXiv:2101.12130 [gr-qc].
- [11] G. Cusin, C. Pitrou, and J.-P. Uzan, Anisotropy of the astrophysical gravitational wave background: Analytic expression of the angular power spectrum and correlation with cosmological observations, Phys. Rev. D **96**, 103019 (2017), arXiv:1704.06184 [astro-ph.CO].
- [12] A. C. Jenkins and M. Sakellariadou, Anisotropies in the stochastic gravitational-wave background: Formalism and the cosmic string case, Phys. Rev. D **98**, 063509 (2018), arXiv:1802.06046 [astro-ph.CO].
- [13] B. P. Abbott *et al.* (LIGO Scientific, Virgo), Search for Tensor, Vector, and Scalar Polarizations in the Stochastic Gravitational-Wave Background, Phys. Rev. Lett. **120**, 201102 (2018), arXiv:1802.10194 [gr-qc].
- [14] T. Callister, A. S. Biscoveanu, N. Christensen, M. Isi, A. Matas, O. Minazzoli, T. Regimbau, M. Sakellariadou, J. Tasson, and E. Thrane, Polarization-based Tests of Gravity with the Stochastic Gravitational-Wave Background, Phys. Rev. X **7**, 041058 (2017), arXiv:1704.08373 [gr-qc].
- [15] N. Seto and A. Taruya, Polarization analysis of gravitational-wave backgrounds from the correlation signals of ground-based interferometers: Measuring a circular-polarization mode, Phys. Rev. D **77**, 103001 (2008), arXiv:0801.4185 [astro-ph].
- [16] R. Kato and J. Soda, Probing circular polarization in stochastic gravitational wave background with pulsar timing arrays, Phys. Rev. D **93**, 062003 (2016), arXiv:1512.09139 [gr-qc].
- [17] B. Allen and A. C. Ottewill, Detection of anisotropies in the gravitational wave stochastic background, Phys. Rev. D **56**, 545 (1997), arXiv:gr-qc/9607068.
- [18] B. Allen and J. D. Romano, Detecting a stochastic background of gravitational radiation: Signal processing strategies and sensitivities, Phys. Rev. D **59**, 102001 (1999), arXiv:gr-qc/9710117.
- [19] J. D. Romano and N. J. Cornish, Detection methods for stochastic gravitational-wave backgrounds: a unified treatment, Living Rev. Rel. **20**, 2 (2017), arXiv:1608.06889 [gr-qc].
- [20] Z. Arzoumanian *et al.* (NANOGrav), The NANOGrav 12.5-year Data Set: Search for Non-Einsteinian Polarization Modes in the Gravitational-wave Background, Astrophys. J. Lett. **923**, L22 (2021), arXiv:2109.14706 [gr-qc].
- [21] G. Agazie *et al.* (NANOGrav), The NANOGrav 15 yr Data Set: Search for Anisotropy in the Gravitational-wave Background, Astrophys. J. Lett. **956**, L3 (2023),

- arXiv:2306.16221 [astro-ph.HE].
- [22] G. Mentasti, C. Contaldi, and M. Peloso, Prospects for detecting anisotropies and polarization of the stochastic gravitational wave background with ground-based detectors, *JCAP* **2023** (08), 053, arXiv:2304.06640 [gr-qc].
- [23] A. G. Abac *et al.* (LIGO Scientific, VIRGO, KAGRA), Cosmological and High Energy Physics implications from gravitational-wave background searches in LIGO-Virgo-KAGRA's O1-O4a runs, arXiv e-prints (2025), arXiv:2510.26848 [gr-qc].
- [24] A. Afzal *et al.* (NANOGrav), The NANOGrav 15 yr Data Set: Search for Signals from New Physics, *Astrophys. J. Lett.* **951**, L11 (2023), [Erratum: *Astrophys. J. Lett.* 971, L27 (2024), Erratum: *Astrophys. J.* 971, L27 (2024)], arXiv:2306.16219 [astro-ph.HE].
- [25] A. G. Abac *et al.* (LIGO Scientific, VIRGO, KAGRA), GWTC-4.0: Population Properties of Merging Compact Binaries, arXiv e-prints (2025), arXiv:2508.18083 [astro-ph.HE].
- [26] G. Agazie *et al.* (NANOGrav), The NANOGrav 15 yr Data Set: Constraints on Supermassive Black Hole Binaries from the Gravitational-wave Background, *Astrophys. J. Lett.* **952**, L37 (2023), arXiv:2306.16220 [astro-ph.HE].
- [27] M. Maggiore, Gravitational wave experiments and early universe cosmology, *Phys. Rept.* **331**, 283 (2000), arXiv:gr-qc/9909001.
- [28] C. Caprini and D. G. Figueroa, Cosmological Backgrounds of Gravitational Waves, *Class. Quant. Grav.* **35**, 163001 (2018), arXiv:1801.04268 [astro-ph.CO].
- [29] R. Caldwell *et al.*, Detection of early-universe gravitational-wave signatures and fundamental physics, *Gen. Rel. Grav.* **54**, 156 (2022), arXiv:2203.07972 [gr-qc].
- [30] J. Gair, J. D. Romano, S. Taylor, and C. M. F. Mingarelli, Mapping gravitational-wave backgrounds using methods from CMB analysis: Application to pulsar timing arrays, *Phys. Rev. D* **90**, 082001 (2014), arXiv:1406.4664 [gr-qc].
- [31] J. R. Gair, J. D. Romano, and S. R. Taylor, Mapping gravitational-wave backgrounds of arbitrary polarisation using pulsar timing arrays, *Phys. Rev. D* **92**, 102003 (2015), arXiv:1506.08668 [gr-qc].
- [32] T. L. Smith and R. Caldwell, Sensitivity to a Frequency-Dependent Circular Polarization in an Isotropic Stochastic Gravitational Wave Background, *Phys. Rev. D* **95**, 044036 (2017), arXiv:1609.05901 [gr-qc].
- [33] S. W. Ballmer, A Radiometer for stochastic gravitational waves, *Class. Quant. Grav.* **23**, S179 (2006), arXiv:gr-qc/0510096.
- [34] S. Mitra, S. Dhurandhar, T. Souradeep, A. Lazzarini, V. Mandic, S. Bose, and S. Ballmer, Gravitational wave radiometry: Mapping a stochastic gravitational wave background, *Phys. Rev. D* **77**, 042002 (2008), arXiv:0708.2728 [gr-qc].
- [35] E. Thrane, S. Ballmer, J. D. Romano, S. Mitra, D. Talukder, S. Bose, and V. Mandic, Probing the anisotropies of a stochastic gravitational-wave background using a network of ground-based laser interferometers, *Physical Review D* **80**, 10.1103/physrevd.80.122002 (2009).
- [36] J. D. Romano, S. R. Taylor, N. J. Cornish, J. Gair, C. M. F. Mingarelli, and R. van Haasteren, Phase-coherent mapping of gravitational-wave backgrounds using ground-based laser interferometers, *Phys. Rev. D* **92**, 042003 (2015), arXiv:1505.07179 [gr-qc].
- [37] R. Abbott *et al.* (KAGRA, Virgo, LIGO Scientific), Search for anisotropic gravitational-wave backgrounds using data from Advanced LIGO and Advanced Virgo's first three observing runs, *Phys. Rev. D* **104**, 022005 (2021), arXiv:2103.08520 [gr-qc].
- [38] N. Anil Kumar, M. Çalıřkan, G. Sato-Polito, M. Kamionkowski, and L. Ji, Linear polarization of the stochastic gravitational-wave background with pulsar timing arrays, *Phys. Rev. D* **110**, 043501 (2024), arXiv:2312.03056 [astro-ph.CO].
- [39] Y.-K. Chu, G.-C. Liu, and K.-W. Ng, Spherical harmonic analysis of anisotropies in polarized stochastic gravitational wave background with interferometry experiments, *Phys. Rev. D* **103**, 063528 (2021), arXiv:2002.01606 [gr-qc].
- [40] G.-C. Liu and K.-W. Ng, Overlap reduction functions for a polarized stochastic gravitational-wave background in the Einstein Telescope-Cosmic Explorer and the LISA-Taiji networks, *Phys. Rev. D* **107**, 104040 (2023), arXiv:2210.16143 [gr-qc].
- [41] N. Anil Kumar and M. Kamionkowski, Efficient Computation of Overlap Reduction Functions for Pulsar Timing Arrays, *Phys. Rev. Lett.* **133**, 151401 (2024), arXiv:2311.14159 [astro-ph.CO].
- [42] J. Suresh, A. Ain, and S. Mitra, Unified mapmaking for an anisotropic stochastic gravitational wave background, *Phys. Rev. D* **103**, 083024 (2021), arXiv:2011.05969 [gr-qc].
- [43] LIGO Scientific Collaboration, Virgo Collaboration, and KAGRA Collaboration, LVK, <https://dcc.ligo.org/LIGO-T2000012/public> (2022).
- [44] K. M. Górski, E. Hivon, A. J. Banday, B. D. Wandelt, F. K. Hansen, M. Reinecke, and M. Bartelman, HEALPix - A Framework for high resolution discretization, and fast analysis of data distributed on the sphere, *Astrophys. J.* **622**, 759 (2005), arXiv:astro-ph/0409513.
- [45] N. Kouvatsos, A. C. Jenkins, A. I. Renzini, J. D. Romano, and M. Sakellariadou, Unbiased estimation of gravitational-wave anisotropies from noisy data, *Phys. Rev. D* **109**, 103535 (2024), arXiv:2312.09110 [astro-ph.CO].
- [46] A. C. Jenkins and M. Sakellariadou, Shot noise in the astrophysical gravitational-wave background, *Phys. Rev. D* **100**, 063508 (2019), arXiv:1902.07719 [astro-ph.CO].
- [47] E. Belgacem, F. Iacovelli, M. Maggiore, M. Mancarella, and N. Muttoni, The spectral density of astrophysical stochastic backgrounds, *JCAP* **04**, 032, arXiv:2411.04028 [gr-qc].
- [48] D. Reitze *et al.*, Cosmic Explorer: The U.S. Contribution to Gravitational-Wave Astronomy beyond LIGO, *Bull. Am. Astron. Soc.* **51**, 035 (2019), arXiv:1907.04833 [astro-ph.IM].
- [49] M. Branchesi *et al.*, Science with the Einstein Telescope: a comparison of different designs, *JCAP* **2023** (07), 068, arXiv:2303.15923 [gr-qc].
- [50] L. Valbusa Dall'Armi, A. Nishizawa, A. Ricciardone, and S. Matarrese, Circular Polarization of the Astrophysical Gravitational Wave Background, *Phys. Rev. Lett.* **131**, 041401 (2023), arXiv:2301.08205 [astro-ph.CO].
- [51] S. Alexander and N. Yunes, Chern-Simons Modified General Relativity, *Phys. Rept.* **480**, 1 (2009), arXiv:0907.2562 [hep-th].
- [52] LIGO Scientific Collaboration, Virgo Collaboration, and KAGRA Collaboration, Folded data for first three observing runs of Advanced LIGO and Advanced Virgo,

Zenodo (2022).

- [53] A. Ain, J. Suresh, and S. Mitra, Very fast stochastic gravitational wave background map making using folded data, *Phys. Rev. D* **98**, 024001 (2018), arXiv:1803.08285 [gr-qc].
- [54] J. T. Whelan, E. L. Robinson, J. D. Romano, and E. H. Thrane, Treatment of Calibration Uncertainty in Multi-Baseline Cross-Correlation Searches for Gravitational Waves, *J. Phys. Conf. Ser.* **484**, 012027 (2014), arXiv:1205.3112 [gr-qc].
- [55] K. Martinovic, C. Badger, M. Sakellariadou, and V. Mandic, Searching for parity violation with the LIGO-Virgo-KAGRA network, *Phys. Rev. D* **104**, L081101 (2021), arXiv:2103.06718 [gr-qc].
- [56] T. Callister, L. Jenks, D. E. Holz, and N. Yunes, New probe of gravitational parity violation through nonobservation of the stochastic gravitational-wave background, *Phys. Rev. D* **111**, 044041 (2025), arXiv:2312.12532 [gr-qc].
- [57] A. Ain, P. Dalvi, and S. Mitra, Fast Gravitational Wave Radiometry using Data Folding, *Phys. Rev. D* **92**, 022003 (2015), arXiv:1504.01714 [gr-qc].
- [58] P. Madau and M. Dickinson, Cosmic Star-Formation History, *Ann. Rev. Astron. Astrophys.* **52**, 415 (2014), arXiv:1403.0007 [astro-ph.CO].

## Supplemental Material (SM)

### S-I. GENERAL DEFINITIONS

Our orthonormal triad, with  $\hat{\Omega}$  depicting the propagation direction of an incoming gravitational wave, is defined as

$$\hat{\Omega}(\theta, \phi) = (\sin \theta \cos \phi, \sin \theta \sin \phi, \cos \theta), \quad (\text{S1})$$

$$\hat{\ell}(\theta, \phi) = (\cos \theta \cos \phi, \cos \theta \sin \phi, -\sin \theta), \quad (\text{S2})$$

$$\hat{m}(\theta, \phi) = (-\sin \phi, \cos \phi, 0), \quad (\text{S3})$$

where  $\theta, \phi$  are the usual spherical coordinates. We adopt the following decomposition of a generic 2-index tensor:

$$e_{ij}^{(+2)}(\hat{\Omega}) = \frac{1}{\sqrt{2}} (\hat{\ell}_i + i\hat{m}_i)(\hat{\ell}_j + i\hat{m}_j), \quad e_{ij}^{(-2)}(\hat{\Omega}) = \frac{1}{\sqrt{2}} (\hat{\ell}_i - i\hat{m}_i)(\hat{\ell}_j - i\hat{m}_j), \quad (\text{S4})$$

$$e_{ij}^{(+1)}(\hat{\Omega}) = -\frac{1}{\sqrt{2}} [(\hat{\ell}_i + i\hat{m}_i)\hat{\Omega}_j + \hat{\Omega}_i(\hat{\ell}_j + i\hat{m}_j)], \quad e_{ij}^{(-1)}(\hat{\Omega}) = -\frac{1}{\sqrt{2}} [(\hat{\ell}_i - i\hat{m}_i)\hat{\Omega}_j + \hat{\Omega}_i(\hat{\ell}_j - i\hat{m}_j)], \quad (\text{S5})$$

$$e_{ij}^{(+0)}(\hat{\Omega}) = \hat{\ell}_i\hat{\ell}_j + \hat{m}_i\hat{m}_j, \quad e_{ij}^{(-0)}(\hat{\Omega}) = \sqrt{2}\hat{\Omega}_i\hat{\Omega}_j. \quad (\text{S6})$$

such that  $\tilde{h}_{ij}(f, \hat{\Omega}) = \sum_{s \in \{\pm 2, \pm 1, \pm 0\}} e_{ij}^{(s)}(\hat{\Omega}) \tilde{h}^{(s)}(f, \hat{\Omega})$ .

Rotation of the triad with the form:

$$\hat{\ell}(\psi) = \cos \psi \hat{\ell} + \sin \psi \hat{m}, \quad (\text{S7})$$

$$\hat{m}(\psi) = -\sin \psi \hat{\ell} + \cos \psi \hat{m} \quad (\text{S8})$$

gives

$$e_{ij}^{(s)}(\hat{\Omega}, \psi) = e^{-is\psi} e_{ij}^{(s)}(\hat{\Omega}), \quad s \in \{\pm 2, \pm 1, \pm 0\}, \quad (\text{S9})$$

hence justifies the labeling as spin/helicity-weight.

We express the detector output in the frequency domain for a time segment labeled by  $t$  as a sum of the GW signal and noise contributions:

$$\tilde{s}_{\mathcal{I}}(f; t) = \tilde{h}_{\mathcal{I}}(f; t) + \tilde{n}_{\mathcal{I}}(f; t). \quad (\text{S10})$$

For a plane wave,

$$h_{ij}(t, \vec{x}) = \int_{-\infty}^{\infty} df \int d\Omega \tilde{h}_{ij}(f, \hat{\Omega}) e^{i2\pi f(t + \hat{\Omega} \cdot \vec{x}/c)}. \quad (\text{S11})$$

In the long-wavelength approximation for a ground-based interferometer (limiting to tensor polarizations),

$$\tilde{h}_{\mathcal{I}}(f; t) = \sum_{A=+, \times} \int_{S^2} d\Omega F_{\mathcal{I}}^A(\hat{\Omega}, t) \tilde{h}_A(f, \hat{\Omega}) e^{i\frac{2\pi f}{c} \hat{\Omega} \cdot \vec{x}_{\mathcal{I}}(t)}, \quad (\text{S12})$$

where  $F_{\mathcal{I}}^A(\hat{\Omega}; t)$  are the antenna pattern functions for polarization  $A \in \{+, \times\}$  and

$$\tilde{h}_{ij}(f, \hat{\Omega}) = \sum_{A=+, \times} e_{ij}^A(\hat{\Omega}) \tilde{h}_A(f, \hat{\Omega}). \quad (\text{S13})$$

In this approximation the  $f$ -dependence of the full response comes only from the phase factor  $e^{i(2\pi f/c)\hat{\Omega} \cdot \vec{x}_{\mathcal{I}}}$  (i.e.  $F_{\mathcal{I}}^A$  is independent of  $f$ ).

For the stochastic background polarization correlations we adopt the Stokes-parameter matrix in  $+/ \times$  basis [19]. Note that the main text Eqs. (2)–(3) use the helicity ( $\pm 2$ ) basis, while here we work in the linear ( $+/ \times$ ) basis; the two are related by a unitary rotation, and the Stokes parameters  $\{I, Q, U, V\}$  are identical in both representations:

$$\langle \tilde{h}_A(f, \hat{\Omega}) \tilde{h}_{A'}^*(f', \hat{\Omega}') \rangle = \frac{1}{2} \delta(f - f') \delta^{(2)}(\hat{\Omega} - \hat{\Omega}') S_h^{AA'}(f, \hat{\Omega}), \quad (\text{S14})$$

with

$$S_h^{AA'}(f, \hat{\Omega}) = \frac{1}{2} \begin{pmatrix} I(f, \hat{\Omega}) + Q(f, \hat{\Omega}) & U(f, \hat{\Omega}) - iV(f, \hat{\Omega}) \\ U(f, \hat{\Omega}) + iV(f, \hat{\Omega}) & I(f, \hat{\Omega}) - Q(f, \hat{\Omega}) \end{pmatrix}_{AA'}. \quad (\text{S15})$$

Using these, and approximating the finite-time delta as  $\delta(0) \rightarrow \tau$  for a segment of duration  $\tau$ , the signal cross-correlation at equal frequency is

$$\begin{aligned} \langle \tilde{h}_{\mathcal{I}}(f; t) \tilde{h}_{\mathcal{J}}^*(f; t) \rangle &= \frac{\tau}{4} \int d\Omega e^{i\frac{2\pi f}{c} \hat{\Omega} \cdot \Delta \vec{x}_{\mathcal{I}\mathcal{J}}(t)} \left[ (F_{\mathcal{I}}^+ F_{\mathcal{J}}^+ + F_{\mathcal{I}}^\times F_{\mathcal{J}}^\times) I + (F_{\mathcal{I}}^+ F_{\mathcal{J}}^+ - F_{\mathcal{I}}^\times F_{\mathcal{J}}^\times) Q \right. \\ &\quad \left. + (F_{\mathcal{I}}^+ F_{\mathcal{J}}^\times + F_{\mathcal{I}}^\times F_{\mathcal{J}}^+) U - i(F_{\mathcal{I}}^+ F_{\mathcal{J}}^\times - F_{\mathcal{I}}^\times F_{\mathcal{J}}^+) V \right], \end{aligned} \quad (\text{S16})$$

where all Stokes parameters and antenna patterns are evaluated at  $(f, \hat{\Omega})$  and

$$\Delta \vec{x}_{\mathcal{I}\mathcal{J}}(t) \equiv \vec{x}_{\mathcal{I}}(t) - \vec{x}_{\mathcal{J}}(t). \quad (\text{S17})$$

It is convenient to define direction-dependent overlap reduction functions (evaluated at a reference time  $t$  over a short segment):

$$\Gamma_{\mathcal{I}\mathcal{J}}^I(f, \hat{\Omega}; t) \equiv \frac{1}{2} \left( F_{\mathcal{I}}^+(\hat{\Omega}, t) F_{\mathcal{J}}^+(\hat{\Omega}, t) + F_{\mathcal{I}}^\times(\hat{\Omega}, t) F_{\mathcal{J}}^\times(\hat{\Omega}, t) \right) e^{i\frac{2\pi f}{c} \hat{\Omega} \cdot \Delta \vec{x}_{\mathcal{I}\mathcal{J}}(t)}, \quad (\text{S18})$$

$$\Gamma_{\mathcal{I}\mathcal{J}}^Q(f, \hat{\Omega}; t) \equiv \frac{1}{2} \left( F_{\mathcal{I}}^+(\hat{\Omega}, t) F_{\mathcal{J}}^+(\hat{\Omega}, t) - F_{\mathcal{I}}^\times(\hat{\Omega}, t) F_{\mathcal{J}}^\times(\hat{\Omega}, t) \right) e^{i\frac{2\pi f}{c} \hat{\Omega} \cdot \Delta \vec{x}_{\mathcal{I}\mathcal{J}}(t)}, \quad (\text{S19})$$

$$\Gamma_{\mathcal{I}\mathcal{J}}^U(f, \hat{\Omega}; t) \equiv \frac{1}{2} \left( F_{\mathcal{I}}^+(\hat{\Omega}, t) F_{\mathcal{J}}^\times(\hat{\Omega}, t) + F_{\mathcal{I}}^\times(\hat{\Omega}, t) F_{\mathcal{J}}^+(\hat{\Omega}, t) \right) e^{i\frac{2\pi f}{c} \hat{\Omega} \cdot \Delta \vec{x}_{\mathcal{I}\mathcal{J}}(t)}, \quad (\text{S20})$$

$$\Gamma_{\mathcal{I}\mathcal{J}}^V(f, \hat{\Omega}; t) \equiv -\frac{i}{2} \left( F_{\mathcal{I}}^+(\hat{\Omega}, t) F_{\mathcal{J}}^\times(\hat{\Omega}, t) - F_{\mathcal{I}}^\times(\hat{\Omega}, t) F_{\mathcal{J}}^+(\hat{\Omega}, t) \right) e^{i\frac{2\pi f}{c} \hat{\Omega} \cdot \Delta \vec{x}_{\mathcal{I}\mathcal{J}}(t)}. \quad (\text{S21})$$

Define also the spin- $\pm 4$  combinations

$$P^\pm(f, \hat{\Omega}) \equiv Q(f, \hat{\Omega}) \pm iU(f, \hat{\Omega}), \quad \Gamma_{\mathcal{I}\mathcal{J}}^\pm(f, \hat{\Omega}; t) \equiv \frac{1}{2} \left( \Gamma_{\mathcal{I}\mathcal{J}}^Q(f, \hat{\Omega}; t) \mp i\Gamma_{\mathcal{I}\mathcal{J}}^U(f, \hat{\Omega}; t) \right), \quad (\text{S22})$$

so that  $\Gamma^Q Q + \Gamma^U U = \Gamma^+ P^+ + \Gamma^- P^-$ .

Spin-weighted spherical harmonics are defined by

$${}_s Y_{\ell m}(\theta, \phi) = (-1)^s \sqrt{\frac{2\ell+1}{4\pi}} D_{m, -s}^{\ell*}(\phi, \theta, 0), \quad \ell \geq |s|, \quad |m| \leq \ell, \quad (\text{S23})$$

with Wigner  $D$ -matrices

$$D_{mm'}^\ell(\alpha, \beta, \gamma) = e^{-im\alpha} d_{mm'}^\ell(\beta) e^{-im'\gamma}, \quad (\text{S24})$$

and normalization

$$\int_{S^2} d\Omega {}_s Y_{\ell m}(\hat{\Omega}) {}_s Y_{\ell' m'}^*(\hat{\Omega}) = \delta_{\ell\ell'} \delta_{mm'}. \quad (\text{S25})$$

We expand each Stokes field in spin-weighted spherical harmonics, writing  $\Omega_X(\hat{\Omega}) = \sum_{\ell m} a_{\ell m}^X {}_s Y_{\ell m}(\hat{\Omega})$  with  $s_X = 0$  for  $X \in \{I, V\}$  and  $s_X = \pm 4$  for  $X = P^\pm$  (so that  $a_{\ell m}^X \equiv \Omega_{\ell m}^X$  in the notation of Eq. (4)).

The gradient ( $E$ ) and curl ( $B$ ) components of the linear polarization are

$$a_{\ell m}^E = -\frac{1}{2}(a_{\ell m}^+ + a_{\ell m}^-), \quad a_{\ell m}^B = \frac{i}{2}(a_{\ell m}^+ - a_{\ell m}^-), \quad (\text{S26})$$

with inverse

$$a_{\ell m}^+ = -a_{\ell m}^E - i a_{\ell m}^B, \quad a_{\ell m}^- = -a_{\ell m}^E + i a_{\ell m}^B. \quad (\text{S27})$$

Under parity  $\hat{\Omega} \rightarrow -\hat{\Omega}$ ,  $E$  is even and  $B$  is odd. The angular power spectra are

$$C_\ell^{XY} = \frac{1}{2\ell+1} \sum_{m=-\ell}^{\ell} \text{Re}[a_{\ell m}^X a_{\ell m}^{Y*}], \quad X, Y \in \{I, V, E, B\}. \quad (\text{S28})$$

For a parity-symmetric background  $C_\ell^{IV} = C_\ell^{IB} = C_\ell^{VE} = C_\ell^{EB} = 0$ .

When presenting O3 pixel-basis upper limits we report the GW energy flux density

$$F_\alpha(\hat{\Omega}) = \frac{c \rho_c}{f_{\text{ref}}} \Omega_\alpha(\hat{\Omega}), \quad (\text{S29})$$

where  $\rho_c = 3H_0^2 c^2 / (8\pi G)$  and  $f_{\text{ref}} = 25$  Hz; all other maps and  $C_\ell$  results are reported as  $\Omega$ .

The corresponding ORFs are

$$\Gamma_{\mathcal{I}\mathcal{J},\ell m}^I(f, t) \equiv \int_{S^2} d\Omega Y_{\ell m}(\hat{\Omega}) \Gamma_{\mathcal{I}\mathcal{J}}^I(f, \hat{\Omega}; t), \quad (\text{S30})$$

$$\Gamma_{\mathcal{I}\mathcal{J},\ell m}^V(f, t) \equiv \int_{S^2} d\Omega Y_{\ell m}(\hat{\Omega}) \Gamma_{\mathcal{I}\mathcal{J}}^V(f, \hat{\Omega}; t), \quad (\text{S31})$$

$$\Gamma_{\mathcal{I}\mathcal{J},\ell m}^+(f, t) \equiv \int_{S^2} d\Omega {}_{+4}Y_{\ell m}(\hat{\Omega}) \Gamma_{\mathcal{I}\mathcal{J}}^+(f, \hat{\Omega}; t), \quad (\text{S32})$$

$$\Gamma_{\mathcal{I}\mathcal{J},\ell m}^-(f, t) \equiv \int_{S^2} d\Omega {}_{-4}Y_{\ell m}(\hat{\Omega}) \Gamma_{\mathcal{I}\mathcal{J}}^-(f, \hat{\Omega}; t). \quad (\text{S33})$$

Combining the above and using orthonormality gives

$$\begin{aligned} \langle \tilde{h}_{\mathcal{I}}(f; t) \tilde{h}_{\mathcal{J}}^*(f; t) \rangle &= \tau \frac{3H_0^2}{4\pi^2 f^3} H(f) \sum_{\ell m} \left[ \Gamma_{\mathcal{I}\mathcal{J},\ell m}^I(f, t) a_{\ell m}^I + \Gamma_{\mathcal{I}\mathcal{J},\ell m}^V(f, t) a_{\ell m}^V \right. \\ &\quad \left. + \Gamma_{\mathcal{I}\mathcal{J},\ell m}^+(f, t) a_{\ell m}^+ + \Gamma_{\mathcal{I}\mathcal{J},\ell m}^-(f, t) a_{\ell m}^- \right]. \end{aligned} \quad (\text{S34})$$

Equivalently, for  $\hat{C}_{\mathcal{I}\mathcal{J}}(f; t) = \tau^{-1} \tilde{s}_{\mathcal{I}}(f; t) \tilde{s}_{\mathcal{J}}^*(f; t)$ ,

$$\langle \hat{C}_{\mathcal{I}\mathcal{J}}(f; t) \rangle = \sum_{\ell m, X} \hat{\Gamma}_{\mathcal{I}\mathcal{J},\ell m}^X(f, t) a_{\ell m}^X, \quad (\text{S35})$$

with  $\hat{\Gamma}_{\mathcal{I}\mathcal{J},\ell m}^X$  defined as the  $\Omega$ -normalized response in the main text.

Exemplary ORFs are given in Fig. S1. The sidereal phase factor  $e^{im\Omega_\oplus(t-t_0)}$  used for data folding (Sec. S-II A) is conventional and we adopt the [19] conventions. Also, we do not attempt to provide analytical expressions for these functions; for a derivation see [39, 40].

## S-II. SIMULATION TESTS

### A. Map-making Validation

We simulate a scenario with stationary Gaussian noise at an expected O5 sensitivity [43] using the LIGO Hanford, LIGO Livingston, and Virgo network. The analysis is performed in both the spherical-harmonic and pixel bases with  $\ell_{\text{max}} = 24$  and HEALPix resolution [44]  $N_{\text{side}} = 8$  ( $N_{\text{pix}} = 768$ ), and three years of data is folded [57] into one sidereal day using  $\Gamma_{\mathcal{I}\mathcal{J},\ell m}^X(f; t) = e^{im\Omega_\oplus(t-t_0)} \Gamma_{\mathcal{I}\mathcal{J},\ell m}^X(f; t_0)$  ( $\Omega_\oplus$  is the Earth's angular rotational velocity). Maps are reported in units  $\Omega_X(f, \hat{\Omega}) \equiv \frac{2\pi^2 f^3}{3H_0^2} X(f, \hat{\Omega})$ , with polarization maps parameterized by  $(p, \chi, \varphi)$  as

$$\begin{aligned} \Omega_Q &= \Omega_I p \sin \chi \cos(4\varphi), \\ \Omega_U &= \Omega_I p \sin \chi \sin(4\varphi), \\ \Omega_V &= \Omega_I p \cos \chi, \end{aligned} \quad (\text{S36})$$

The simulation consists of an unpolarized galactic plane (band half-width  $10^\circ$  about the great circle with pole at  $(\theta, \phi) = (45^\circ, 0^\circ)$ , where  $\theta$  is colatitude) with  $\Omega_I(f) = 10^{-6} (f/25 \text{ Hz})^{-7/3}$ , a circularly polarized cap centered at  $(\theta, \phi) = (90^\circ, 90^\circ)$  of radius  $12^\circ$  with  $(p, \chi, \varphi) = (0.8, 0^\circ, 0^\circ)$ , and a linearly polarized cap centered at  $(\theta, \phi) = (90^\circ, 270^\circ)$  of radius  $12^\circ$  with  $(p, \chi, \varphi) = (0.8, 90^\circ, 40^\circ)$ .

In this realization (Fig. S2), the full-Stokes reconstruction recovers the simulated unpolarized plane in  $I$  and the polarized caps in  $V$  and  $Q/U$  in both the pixel and spherical-harmonic implementations. Using the standard

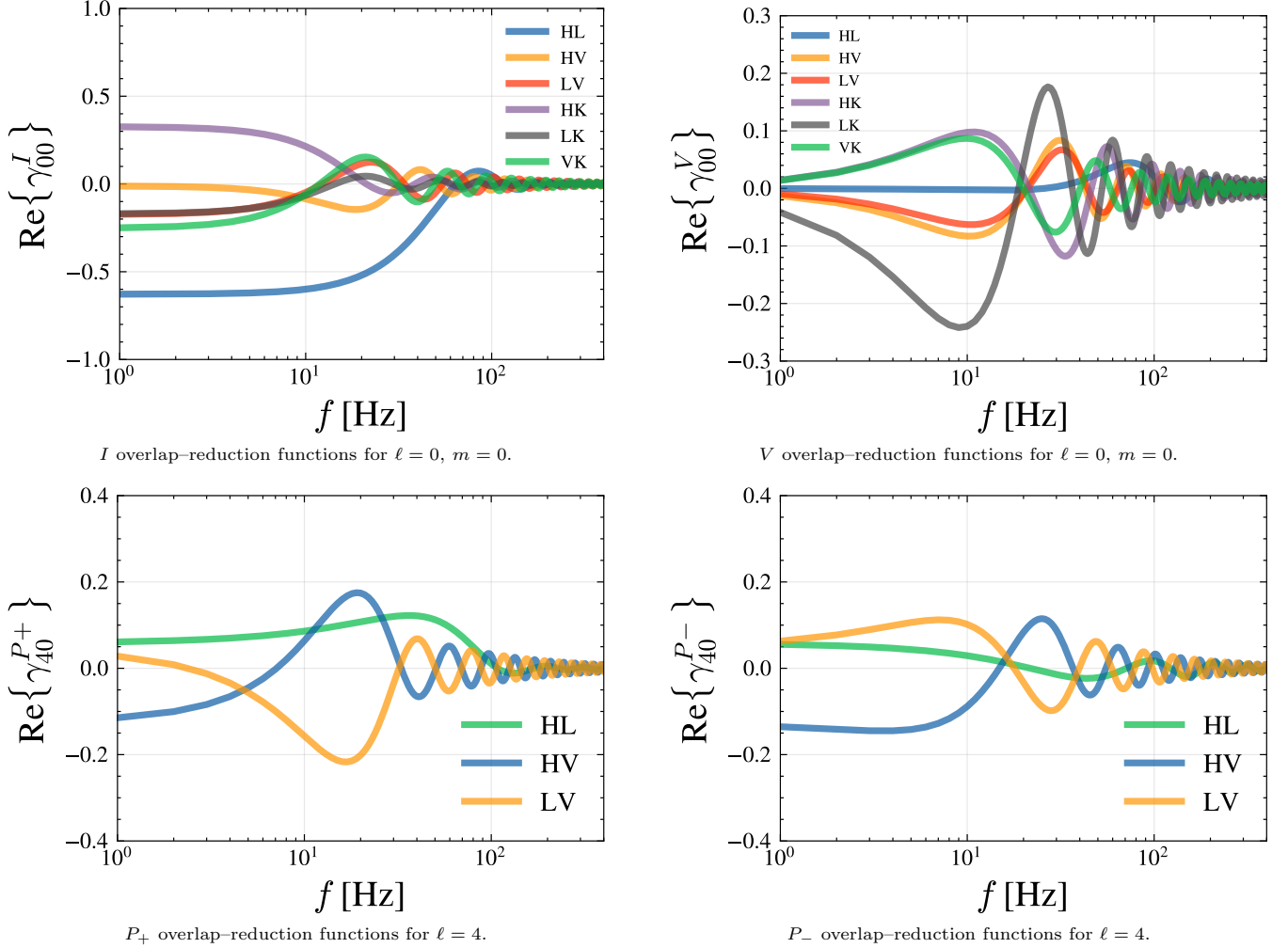


FIG. S1. Real parts of the ORFs  $\gamma_{\ell m}^X(f) = 1/\sqrt{4\pi} \Gamma_{\ell m}^X(f)$  normalized with the conventions in [19] for selected modes and polarizations. Imaginary parts of ORF's vanish for  $m = 0$ .

map-making estimator  $\hat{a} = \mathcal{F}^{-1} \hat{\mathcal{X}}$ , we define the coefficient covariance  $\Sigma \equiv \text{Cov}(\hat{a}) = \mathcal{F}_{\text{reg}}^{-1}$ , where  $\mathcal{F}_{\text{reg}}^{-1}$  is the eigenvalue-threshold pseudo-inverse of  $\mathcal{F} = U \text{diag}(\lambda_i) U^\dagger$ , retaining only modes with  $\lambda_i/\lambda_{\text{max}} \geq r_{\text{cond}}$ . We adopt  $r_{\text{cond}} = 10^{-5}$  as a representative cutoff that removes poorly constrained modes while retaining the large-scale features of interest; moderate variations in  $r_{\text{cond}}$  ( $10^{-4}$ – $10^{-6}$ ) leave the qualitative structure unchanged, affecting only the expected variance–resolution tradeoff.

We denote the reconstructed pixelized Stokes maps by  $\hat{m}_p^X$  ( $X \in \{I, V, Q, U\}$ ), with  $\hat{m}_p^X \equiv \hat{a}_p^X$  in the pixel basis and  $\hat{m}_p^X$  obtained by harmonic synthesis of  $\hat{a}_{\ell m}^X$  on the same grid in the spherical-harmonic basis. Propagating  $\Sigma$  to map space gives  $\Sigma^{(m)} \equiv \text{Cov}(\hat{m})$  and the per-pixel  $1\sigma$  uncertainty map  $\sigma_p^X \equiv \sqrt{(\Sigma^{(m)})_{pp}^{XX}}$ , from which we form the normalized residual and SNR maps,  $(\hat{m}_p^X - m_{\text{true},p}^X)/\sigma_p^X$  and  $\text{SNR}_p^X \equiv \hat{m}_p^X/\sigma_p^X$ . As shown in Fig. S2 and Fig. S3, the plane reaches per-pixel  $\text{SNR} \sim \mathcal{O}(10)$  while the polarized caps reach  $\text{SNR} \sim \mathcal{O}(1-10)$ , with  $Q$  most significant (and  $U$  lower, consistent with the simulated  $\varphi = 40^\circ$ ). The SH maps appear somewhat grainier than the pixel versions, most noticeably for  $U$  which has the smallest simulated amplitude; this reflects the different sets of modes retained by the eigenvalue-threshold regularization in the two parameterizations. Repeating the analysis with the standard  $I$ -only pipeline yields residuals that deviate from noise and a clean  $I$  map biased relative to the simulated intensity (Fig. S4); see Sec. S-II B for representative map-level diagnostics.

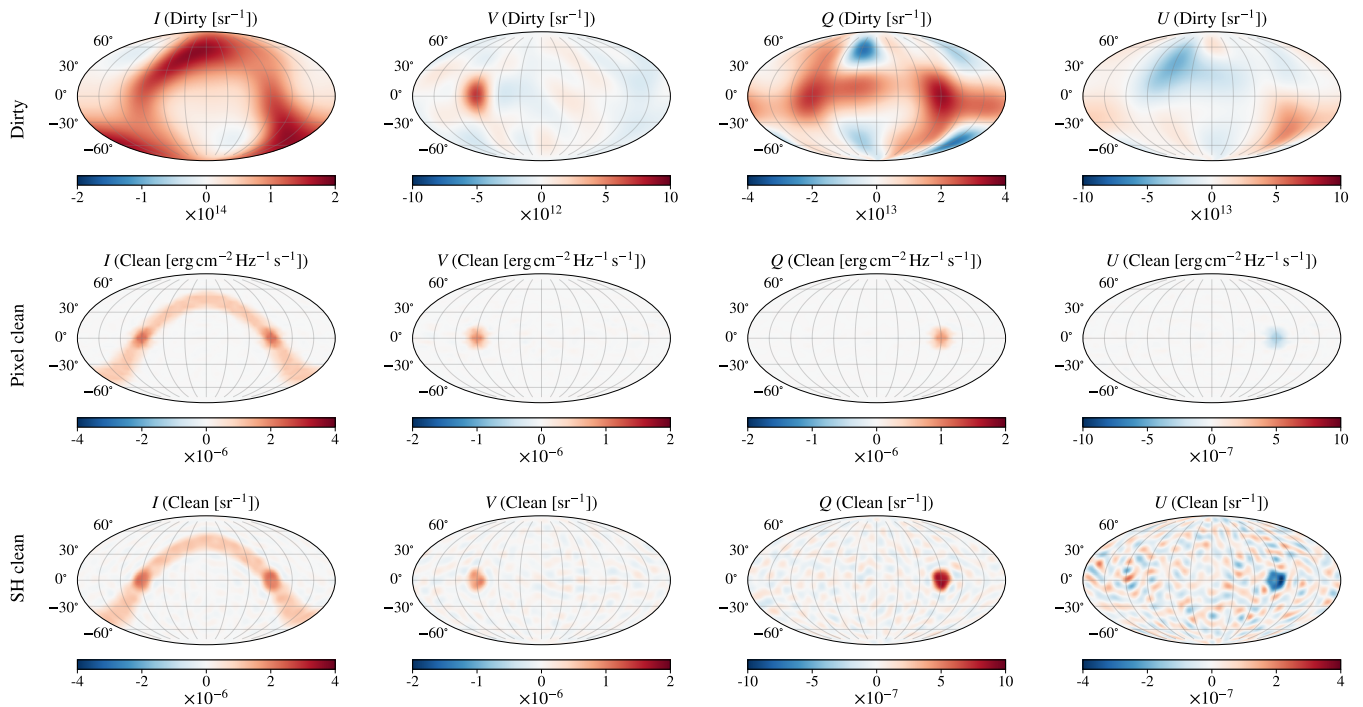


FIG. S2. Benchmark full-Stokes map making for the simulated polarized background using the HLV network (three years;  $\ell_{\max} = 24$ ;  $N_{\text{side}} = 8$ ). Columns show the reconstructed Stokes components  $I$ ,  $V$ ,  $Q$ , and  $U$  in a Mollweide projection (coordinates are colatitude  $\theta$  and longitude  $\phi$ , with latitude  $b = 90^\circ - \theta$ ). The three rows compare the network dirty maps  $\hat{\mathcal{X}}$  to the corresponding clean maps in the pixel and spherical-harmonic bases; both bases recover the simulated morphology: an unpolarized band (half-width  $10^\circ$ ) about the great circle with pole at  $(\theta, \phi) = (45^\circ, 0^\circ)$ , a circularly polarized cap in  $V$  centered at  $(90^\circ, 90^\circ)$  with radius  $12^\circ$  and  $(p, \chi, \varphi) = (0.8, 0^\circ, 0^\circ)$ , and a linearly polarized cap in  $Q/U$  centered at  $(90^\circ, 270^\circ)$  with radius  $12^\circ$  and  $(p, \chi, \varphi) = (0.8, 90^\circ, 40^\circ)$  (giving a stronger  $Q$  feature than  $U$ ).

## B. I-only Comparison

To illustrate the polarization-induced bias directly in map space, we compare the recovered intensity clean map  $\hat{m}^I$  and the normalized residual  $(\hat{m}^I - m_{\text{true}}^I)/\sigma^I$  for the benchmark simulation described in Sec. S-II A, for both the full-Stokes and  $I$ -only analyses (with  $\sigma^I$  the per-pixel uncertainty propagated from the Fisher-matrix covariance). In the full-Stokes reconstruction the residual-over- $\sigma$  map is consistent with noise, with fluctuations centered near zero and typical excursions at the  $\sim 2\sigma$  level. In contrast, the  $I$ -only reconstruction shows coherent extended regions where the residual significantly exceeds the nominal uncertainty, providing a map-level visualization of how neglected polarized anisotropies leak into the inferred intensity.

## C. Network Conditioning Tests

In this section we present a benchmark designed to illustrate how the conditioning of the map-making inverse problem depends on network geometry. We consider a stylized “SGWB” sky consisting of four compact features labeled  $\{S, W, G, B\}$ :  $S$  is unpolarized (intensity only),  $W$  is predominantly circularly polarized, and  $G/B$  are partially linearly polarized. We analyze three years of folded data in the spherical-harmonic basis with  $\ell_{\max} = 24$ .

As in Sec. S-II, Fisher-matrix inversions are regularized via an eigenvalue-threshold pseudo-inverse. Writing  $\mathcal{F} = U \text{diag}(\lambda_i) U^\dagger$ , we retain only modes with  $\lambda_i/\lambda_{\max} \geq r_{\text{cond}}$  and take  $r_{\text{cond}} = 10^{-5}$  as a representative benchmark. We compare three detector networks with decreasing baseline coverage: HLVK, HLV, and HL with expected O5 sensitivity [43]. The resulting recovered maps are shown in Fig. S5; the qualitative recovery visibly degrades as baselines are removed, consistent with increased degeneracy in the inversion of Fisher matrix.

To quantify this behavior independent of map amplitudes, Fig. S6 shows the sorted Fisher eigenvalue spectra for these cases, with each spectrum normalized by its maximum eigenvalue. Adding baselines increases the number of

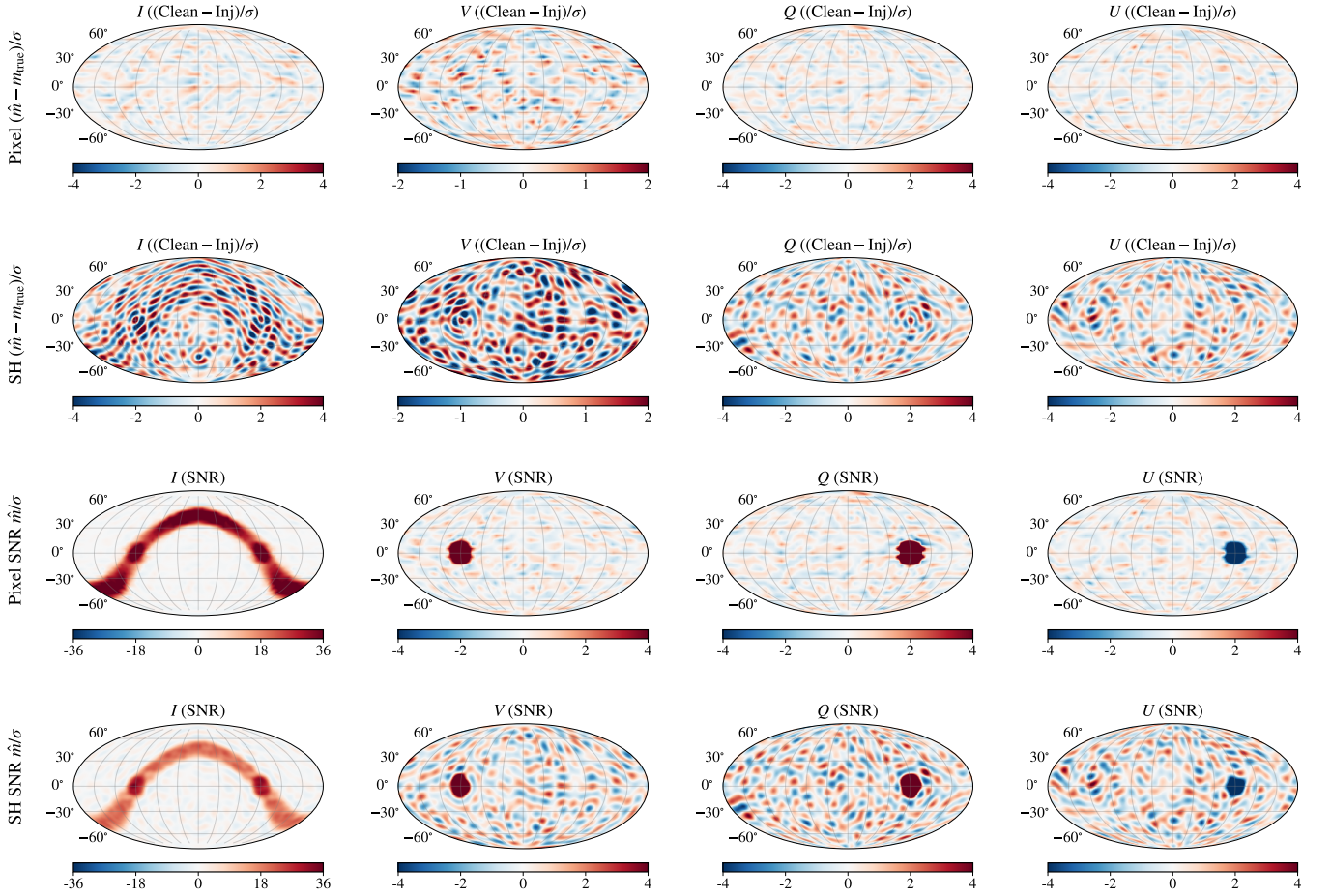


FIG. S3. Benchmark full-Stokes map making (continued). The rows quantify reconstruction accuracy using the per-pixel uncertainty  $\sigma_p^X \equiv \sqrt{(\boldsymbol{\Sigma}^{(m)})_{pp}^{XX}}$  obtained by propagating the regularized coefficient covariance  $\boldsymbol{\Sigma} = \mathcal{F}_{\text{reg}}^{-1}$ . We show normalized residuals  $(\hat{m}_p^X - m_{\text{true},p}^X) / \sigma_p^X$  and the corresponding SNR maps  $\text{SNR}_p^X \equiv \hat{m}_p^X / \sigma_p^X$  for each basis. The residual-over- $\sigma$  maps are consistent with noise for the full-Stokes solution, while the SNR maps highlight the high-significance recovery of the plane in  $I$  and the polarized caps (see the text).

modes above the regularization threshold and hence increases the effective rank of the reconstruction. We show both the full-Stokes Fisher matrix and, for comparison, the intensity-only ( $I$ -block) Fisher matrix, highlighting that the strongest conditioning gains from additional baselines typically occur in the full-Stokes system.

### S-III. INTENSITY COVARIANCE IN THE FULL-STOKES ANALYSIS

Here we derive the result quoted in the main text: for an unregularized full-rank fit, the intensity covariance in the full Stokes fit is larger than or equal to that of the intensity-only fit.

We split the clean-map parameters as  $\mathbf{a} = (\mathbf{a}_I, \mathbf{a}_Y)$  with  $Y \in \{V, +, -\}$  and write the Fisher matrix and dirty map in block form

$$\mathcal{F} = \begin{pmatrix} \mathcal{F}_{II} & \mathcal{F}_{IY} \\ \mathcal{F}_{YI} & \mathcal{F}_{YY} \end{pmatrix}, \quad \mathcal{X} = \begin{pmatrix} \mathcal{X}_I \\ \mathcal{X}_Y \end{pmatrix}. \quad (\text{S37})$$

The usual anisotropic analysis keeps only the intensity block,

$$\hat{\mathbf{a}}_I^{(I\text{-only})} = \mathcal{F}_{II}^{-1} \mathcal{X}_I, \quad \Sigma^{II, (I\text{-only})} = \mathcal{F}_{II}^{-1}. \quad (\text{S38})$$

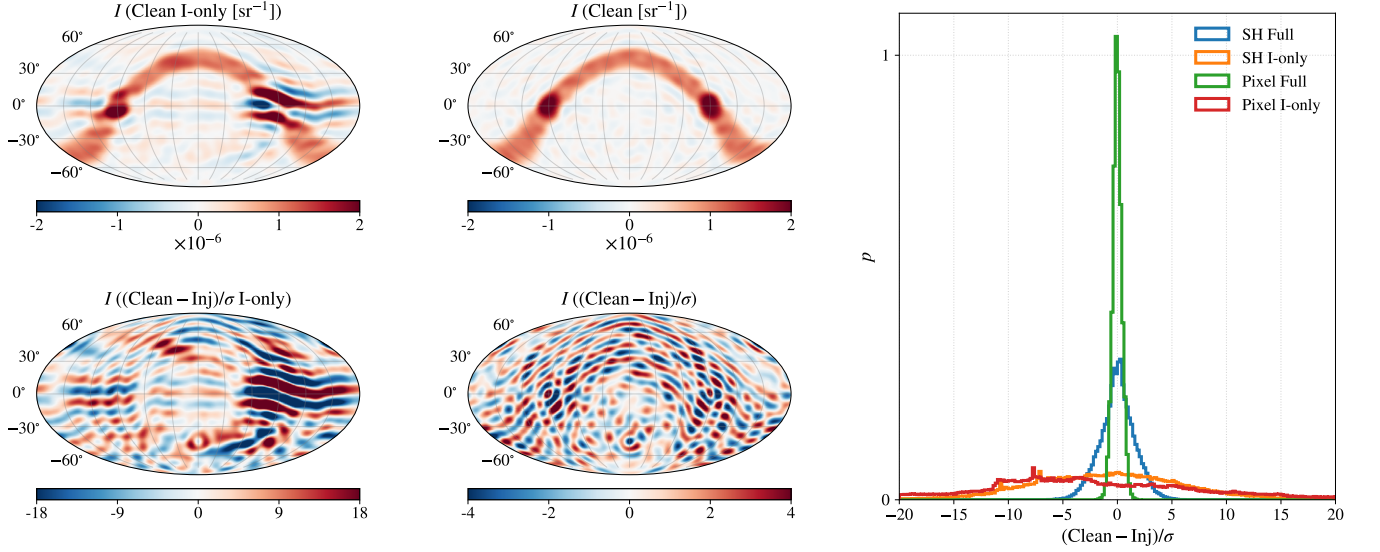


FIG. S4.  $I$ -only versus full-Stokes reconstruction for the benchmark scenario. *Left column:*  $I$ -only analysis; *center column:* full-Stokes analysis. Top row shows the clean intensity map  $\hat{m}^I$ , bottom row shows the normalized residual  $(\hat{m}^I - m_{\text{true}}^I)/\sigma^I$  (note the different color scales:  $\pm 18$  for  $I$ -only vs.  $\pm 4$  for full-Stokes). *Right:* histogram of the per-pixel normalized residual for the  $I$  Stokes parameter across both basis representations and analysis types.

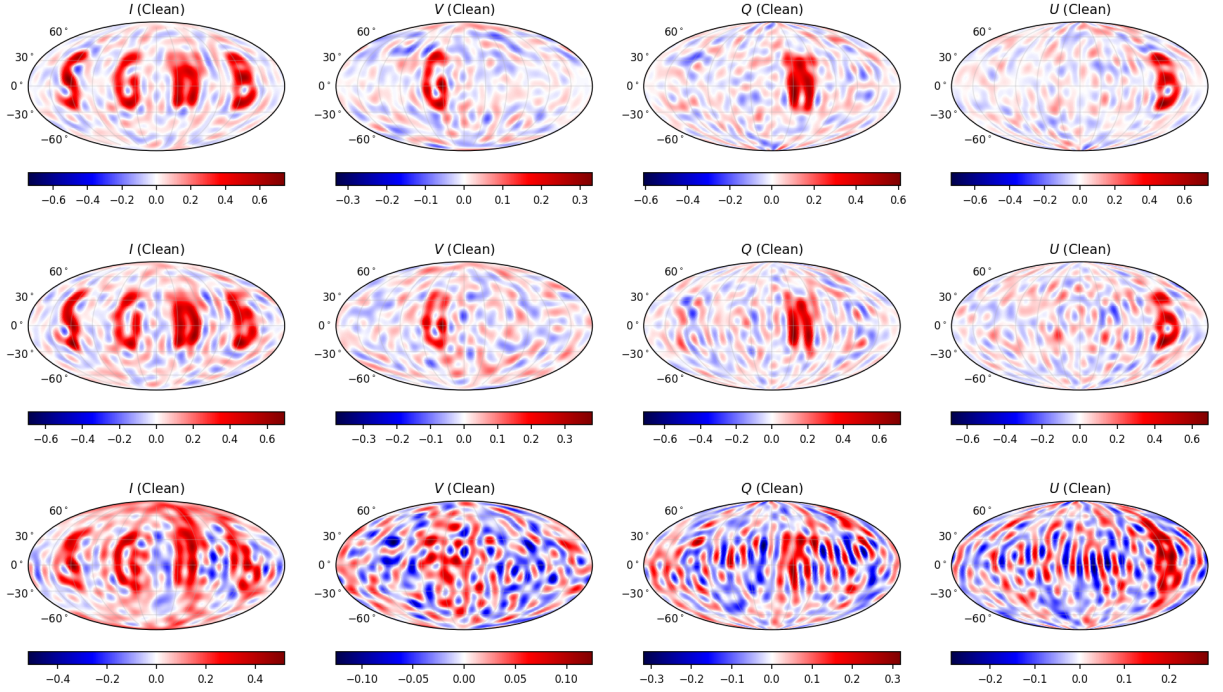


FIG. S5. Example simulation in the spherical-harmonic basis for different detector networks (top to bottom: HLVK, HL, HL) with  $\ell_{\text{max}} = 24$  and  $r_{\text{cond}} = 10^{-5}$ . Color scales are chosen for visual clarity rather than absolute calibration. Fig. S6 quantifies the corresponding conditioning via the Fisher-eigenvalue spectra.

In the full analysis the intensity block of the inverse Fisher matrix is given by the Schur complement

$$\mathbb{S} \equiv \mathcal{F}_{II} - \mathcal{F}_{IY} \mathcal{F}_{YY}^{-1} \mathcal{F}_{YI}, \quad (\text{S39})$$

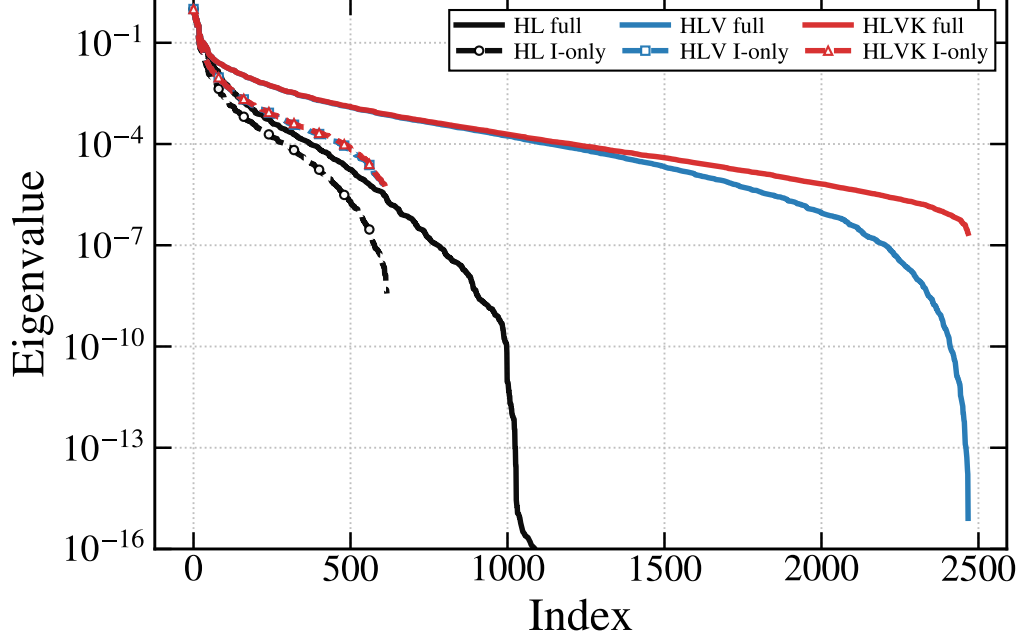


FIG. S6. Sorted eigenvalues of the Fisher matrix for the different networks (HLVK, HLV, HL), each normalized by its maximum eigenvalue. Solid curves show the full-Stokes Fisher matrix; dashed curves show the intensity-only ( $I$ -block) Fisher matrix. Adding baselines increases the number of modes above threshold (improved conditioning/effective rank), with the strongest gains from the addition of Virgo.

so that

$$\hat{\mathbf{a}}_I^{(\text{full})} = \mathbb{S}^{-1} (\mathcal{X}_I - \mathcal{F}_{IY} \mathcal{F}_{YY}^{-1} \mathcal{X}_Y), \quad \Sigma^{II,(\text{full})} = \mathbb{S}^{-1}. \quad (\text{S40})$$

The term  $\mathcal{F}_{IY} \mathcal{F}_{YY}^{-1} \mathcal{X}_Y$  subtracts the polarization contribution leaked into the intensity dirty map via the off-diagonal Fisher blocks.

To compare the covariances, we write

$$\mathbb{S} = \mathcal{F}_{II}^{1/2} (\mathbb{I} - M) \mathcal{F}_{II}^{1/2}, \quad (\text{S41})$$

$$M \equiv \mathcal{F}_{II}^{-1/2} \mathcal{F}_{IY} \mathcal{F}_{YY}^{-1} \mathcal{F}_{YI} \mathcal{F}_{II}^{-1/2}. \quad (\text{S42})$$

The matrix  $M$  is Hermitian and positive semi-definite: defining  $B \equiv \mathcal{F}_{YY}^{-1/2} \mathcal{F}_{YI} \mathcal{F}_{II}^{-1/2}$  we can write  $M = B^\dagger B$ , so all its eigenvalues are real and non-negative. For an unregularized full-rank fit,  $\mathcal{F}$  is positive definite on the fitted parameter space. The Schur complement  $\mathbb{S}$  is then positive definite, which implies that all eigenvalues of  $M$  are strictly smaller than one and  $\mathbb{I} - M$  is positive definite.

The intensity covariance in the full fit is then

$$\Sigma^{II,(\text{full})} = \mathbb{S}^{-1} = \mathcal{F}_{II}^{-1/2} (\mathbb{I} - M)^{-1} \mathcal{F}_{II}^{-1/2} \quad (\text{S43})$$

$$= \mathcal{F}_{II}^{-1} + \mathcal{F}_{II}^{-1/2} [(\mathbb{I} - M)^{-1} - \mathbb{I}] \mathcal{F}_{II}^{-1/2}. \quad (\text{S44})$$

Diagonalizing  $M$  as  $M = U \Lambda U^\dagger$  with eigenvalues  $\lambda_i \in [0, 1)$ , we see that the eigenvalues of  $(\mathbb{I} - M)^{-1} - \mathbb{I}$  are

$$\frac{1}{1 - \lambda_i} - 1 = \frac{\lambda_i}{1 - \lambda_i} \geq 0, \quad (\text{S45})$$

so  $(\mathbb{I} - M)^{-1} - \mathbb{I}$  is positive semi-definite. Therefore the second term in the last line is a positive semi-definite matrix, and we conclude that  $\Sigma^{II,(\text{full})} - \Sigma^{II,(I\text{-only})}$  is positive semi-definite as well.

Thus the full covariance is equal to the intensity-only covariance plus an extra non-negative contribution. Any linear combination of intensity multipoles therefore has an uncertainty in the full fit that is greater than or equal to the corresponding uncertainty in the intensity-only fit, as stated in the main text (see [31] for the PTA context of this generic behavior).

#### S-IV. O3 SUPPLEMENTARY RESULTS

Figure S7 presents the full-Stokes O3 sky maps for  $\alpha = 0$  and  $\alpha = 3$ , complementing the  $\alpha = 2/3$  results of Fig. 3. We find no statistically significant anisotropy in any Stokes parameter at any spectral index; the polarized channels are therefore reported as upper limits throughout this section.

##### A. Significance and upper-limit construction

The global significance of the per-pixel statistics defined in the main text (SNR for  $I, V$  and  $\rho_P$  for linear polarization) comes from a noise-only Monte Carlo with the full Fisher covariance: we draw  $X_{\text{noise}} \sim \mathcal{N}(0, \Gamma)$  by colouring white noise with the SVD of  $\Gamma$ , recompute the sky maximum ( $T = \max_{\hat{n}} |\text{SNR}|$  for  $I, V$  and  $T = \max_{\hat{n}} \rho_P$  for  $P$ ) for each of  $N_{\text{MC}} = 2 \times 10^4$  realizations, and report  $p_{\text{glob}} = (1 + \#\{T_{\text{MC}} \geq T_{\text{obs}}\}) / (1 + N_{\text{MC}})$ . This null carries the sky-correlation look-elsewhere correction. The 95% flux upper limits are flat non-negative Bayesian limits with the per-detector amplitude calibration marginalized as in Ref. [54]. Each detector  $\mathcal{I}$  carries a calibration factor  $\lambda_{\mathcal{I}} \sim \mathcal{N}(1, \delta_{\mathcal{I}}^2)$ , with  $\delta_{\mathcal{I}} \in \{0.048, 0.054\}$  (O1 H/L),  $\{0.026, 0.0385\}$  (O2 H/L) and  $\{0.0696, 0.0637, 0.050\}$  (O3 H/L/V) [10, 37]. Baseline factors  $\lambda_{\mathcal{I}\mathcal{J}} = \lambda_{\mathcal{I}}\lambda_{\mathcal{J}}$  share detectors, so we marginalize the joint per-baseline Gaussian likelihood for  $\hat{F}_{\mathcal{I}\mathcal{J}}$  over  $\lambda_{\mathcal{I}}$  by Monte Carlo with  $N_{\lambda} = 800$  draws, and report the 95% quantile as the upper limit. For  $P = \sqrt{Q^2 + U^2}$  the  $Q$  and  $U$  estimates enter jointly with the polarization angle marginalized analytically. Figure S8 shows the resulting null distributions and observed statistics.

The SPH analysis follows the LVK SVD regularization of Refs. [37, 42, 53], discarding the smallest 1/3 of the Fisher eigenmodes at  $\ell_{\text{max}} = 3, 4, 16$  for  $\alpha = 0, 2/3, 3$ , with the angular-power estimator of Eq. (8) extended over Stokes indices  $X, Y \in \{I, V, E, B\}$ .

For each Stokes spectrum we test whether any harmonic mode shows significant deviation from noise. The clean-map coefficients  $\hat{\Omega}_{\ell m}$  are complex, with Re/Im variances  $\sigma_{\text{Re}, \ell m}^2$  and  $\sigma_{\text{Im}, \ell m}^2$  following from the Fisher inverse [37]. We form

$$z_{\ell m}^{\text{Re}} = \frac{\text{Re} \hat{\Omega}_{\ell m}}{\sigma_{\text{Re}, \ell m}}, \quad z_{\ell m}^{\text{Im}} = \frac{\text{Im} \hat{\Omega}_{\ell m}}{\sigma_{\text{Im}, \ell m}}, \quad (\text{S46})$$

and take the largest  $|z|$  across all modes as the test statistic. These are standardized mode by mode, but the Fisher inversion correlates them and broadens the null, so we obtain the distribution of  $\max |z|$  directly by Monte Carlo rather than assuming a Gaussian form. We draw  $5 \times 10^4$  dirty-map realizations  $\hat{\mathcal{X}}_{\text{sim}} \sim \mathcal{CN}(0, \mathcal{F})$ , pass each through the same Fisher inversion, and record the maximum  $|z|$ . Comparing the observed maximum to this empirical null gives the global  $p$ -value  $p_{\text{glob}}$ . With a 5% detection threshold we find  $p_{\text{glob}} \in [0.06, 0.81]$  across  $\alpha \in \{0, 2/3, 3\}$  and Stokes spectra, with no spectrum crossing threshold (Fig. S9).

The angular-power upper limits for the auto spectra use the same flat non-negative Bayesian construction as the pixel analysis, with the calibration marginalized in the same way. For the  $IV$  cross spectrum, which is signed, we quote the corresponding 95% bound on  $|C_{\ell}^{IV}|$ . Since  $C_{\ell} \propto \lambda^2$ , the per-baseline calibration factors  $\lambda_{\mathcal{I}\mathcal{J}}$  enter the posterior through an  $\ell$ -dependent response

$$b_{\ell}(\lambda) = \frac{\sum_{ab} |\sum_{\mathcal{I}\mathcal{J}} \lambda_{\mathcal{I}\mathcal{J}} (G_{\ell}^{\mathcal{I}\mathcal{J}})_{ab}|^2}{\sum_{ab} |\sum_{\mathcal{I}\mathcal{J}} (G_{\ell}^{\mathcal{I}\mathcal{J}})_{ab}|^2}, \quad G^{\mathcal{I}\mathcal{J}} = \Sigma \mathcal{F}_{\mathcal{I}\mathcal{J}}, \quad (\text{S47})$$

that weights each baseline's contribution to the multipole; the indices  $a, b$  run over the entries of the  $(2\ell + 1)$ -mode block  $G_{\ell}^{\mathcal{I}\mathcal{J}}$ . The posterior is

$$P(C_{\ell} | \hat{C}_{\ell}) \propto \langle \mathcal{N}(\hat{C}_{\ell}; b_{\ell}(\lambda) C_{\ell}, \sigma_{\ell}^2) \rangle_{\lambda}, \quad C_{\ell} \geq 0, \quad (\text{S48})$$

with the per-detector  $\lambda_{\mathcal{I}}$  marginalized by Monte Carlo as for the pixel limits; its 95% quantile is the upper limit. Figure S10 gives the full-Stokes  $II, VV, EE, BB$  and  $|IV|$  upper limits for  $\alpha = 0$  and  $\alpha = 3$ , and Fig. S11 the corresponding point estimates.

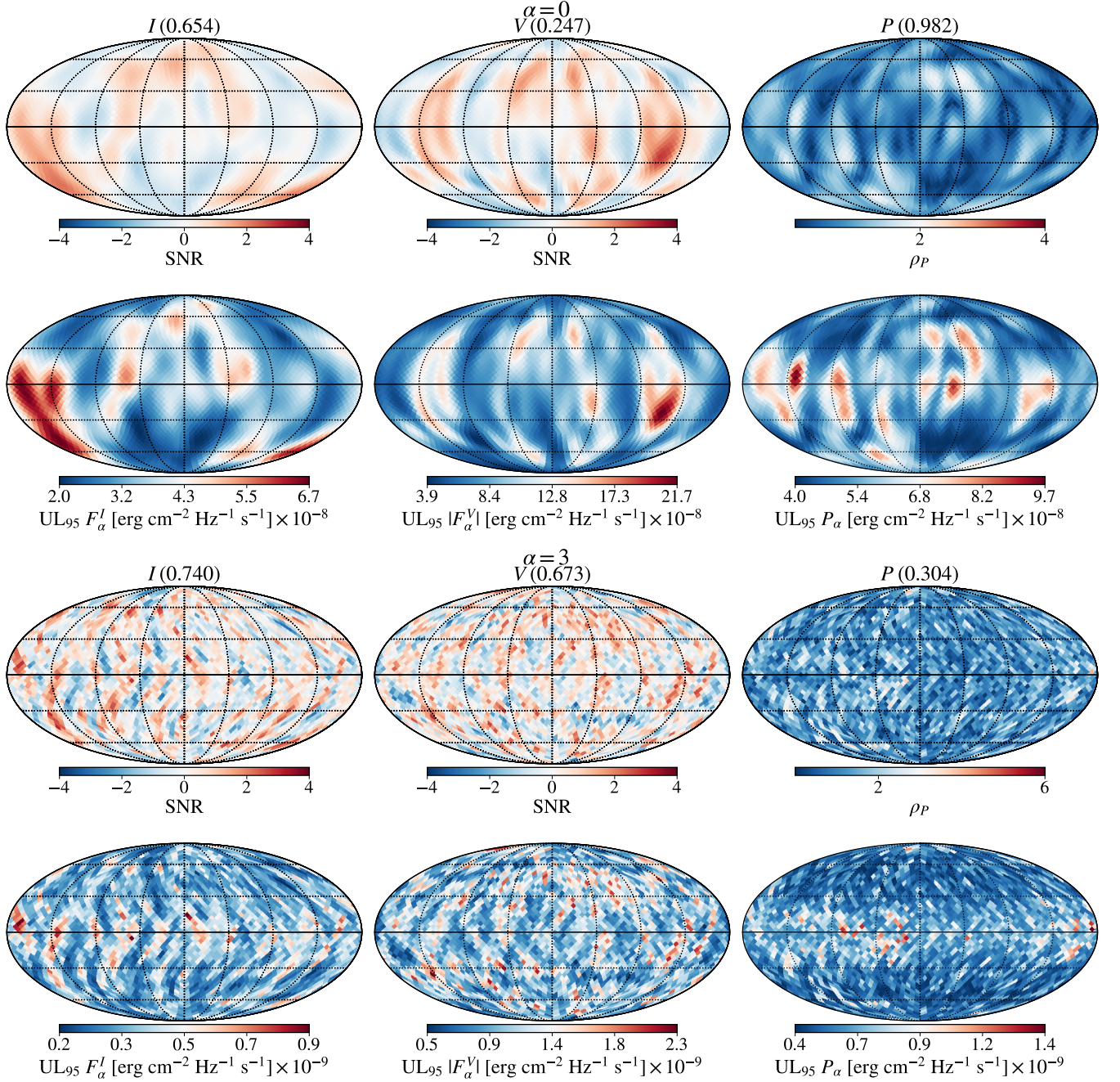


FIG. S7. Full-Stokes O3 sky maps. The two upper rows correspond to  $\alpha = 0$  and the two lower rows to  $\alpha = 3$ . In each pair the first row is the per-pixel SNR for  $I$ ,  $V$  and the linear-polarization significance  $\rho_P$ , and the second row is the corresponding 95% upper limit on the GW energy-flux density  $F_{\alpha}^I$ ,  $|F_{\alpha}^V|$  and  $P_{\alpha} = \sqrt{Q^2 + U^2}$  in erg cm $^{-2}$  Hz $^{-1}$  s $^{-1}$ . Maps use  $N_{\text{side}} = 16$ ; the significance and upper-limit construction is detailed in Sec. S-IV A.

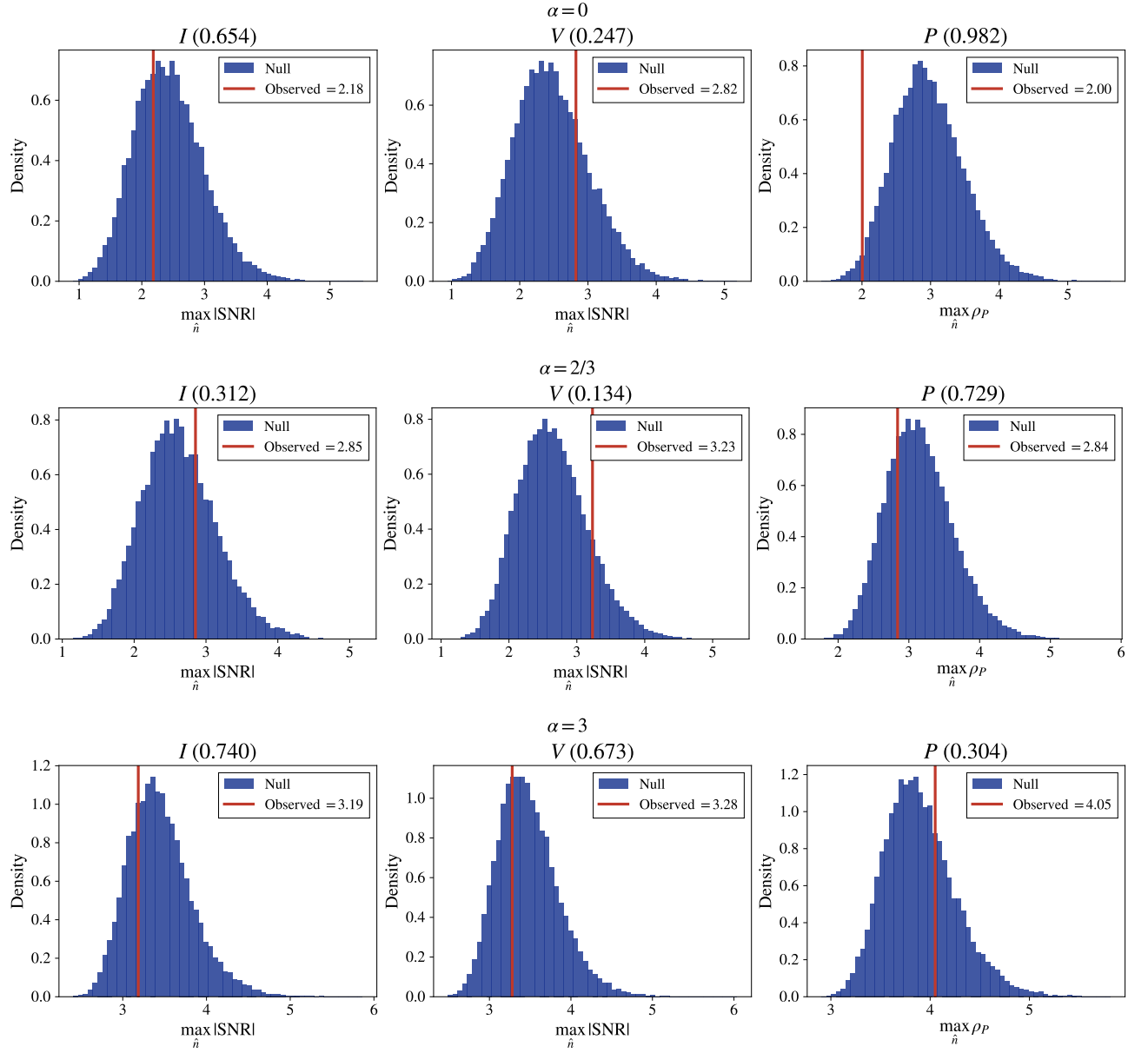


FIG. S8. Pixel-basis global significance. From top to bottom the rows are  $\alpha = 0, 2/3$  and  $3$ ; each row shows the  $I, V$  and  $P$  channels. The histogram is the noise-only null distribution of the sky maximum statistic ( $\max_{\hat{n}} |\text{SNR}|$  for  $I, V$  and  $\max_{\hat{n}} \rho_P$  for  $P$ ) and the vertical line the observed value for our analysis.  $p_{\text{glob}}$  is the fraction of null realizations at or above this value.

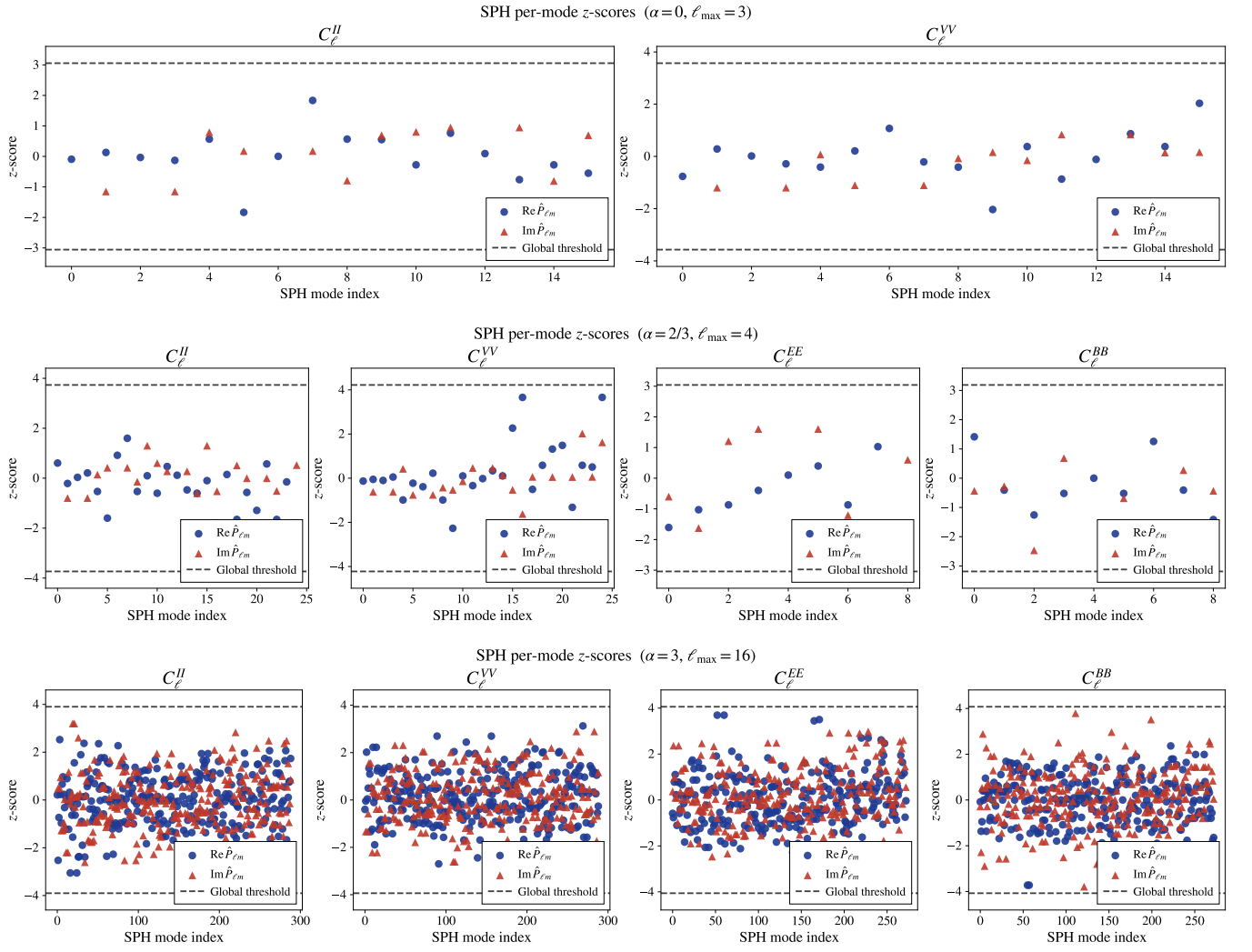


FIG. S9. SPH per-mode z-scores; rows are  $\alpha = 0, 2/3$  and  $3$  with  $\ell_{\max} = 3, 4, 16$  from top to bottom. Circles and triangles are the real and imaginary parts of  $\hat{\Omega}_{\ell m}$ ; the dashed line is the 5% quantile of the null  $|z|$  distribution.

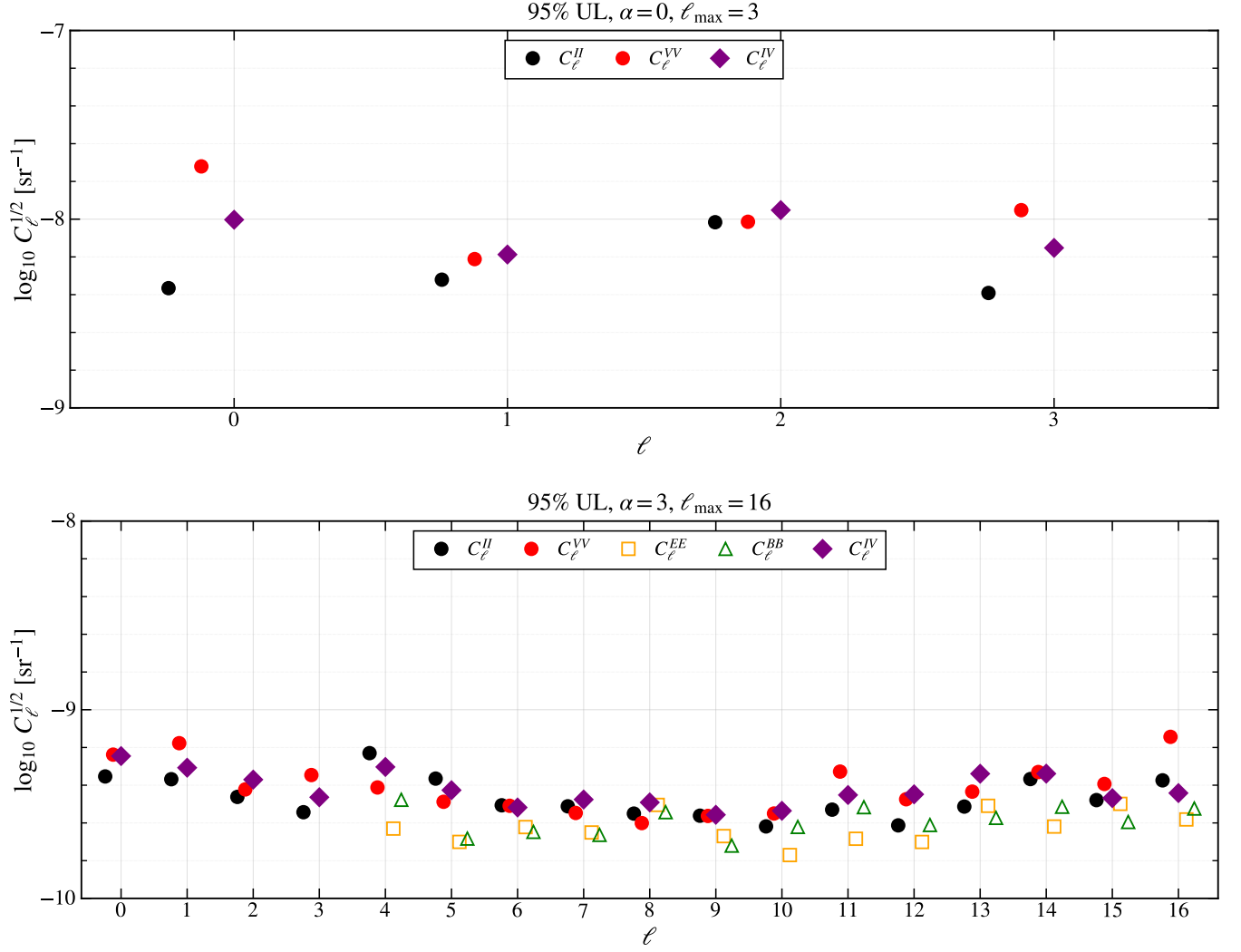


FIG. S10. Full-Stokes SPH 95% upper limits  $\log_{10} C_{\ell}^{1/2} [\text{sr}^{-1}]$  for  $\alpha = 0$  with  $\ell_{\max} = 3$  on top and  $\alpha = 3$  with  $\ell_{\max} = 16$  on the bottom, complementing the  $\alpha = 2/3$  result of Fig. 3. The  $E$  and  $B$  spectra start at  $\ell = 4$ .

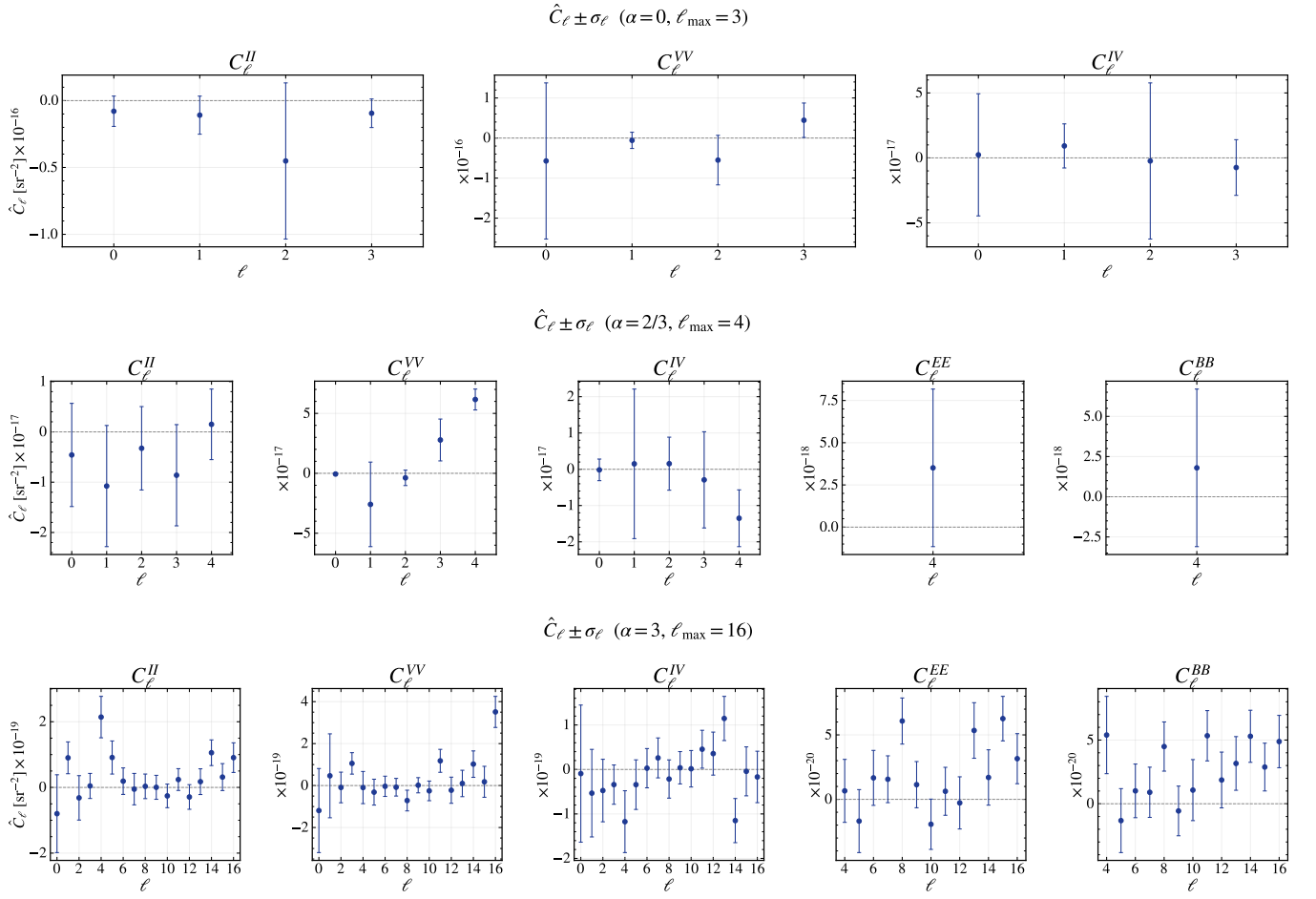


FIG. S11. SPH angular-power point estimates  $\hat{C}_\ell \pm \sigma_\ell$  on a linear scale, where the estimator can be negative; rows are  $\alpha = 0, 2/3$  and  $3$  from top to bottom. All spectra are consistent with zero at the  $2\sigma$  level, so only upper limits are quoted. The  $E$  and  $B$  spectra are defined for  $\ell \geq 4$ .

### S-V. CBC POPULATION AND SHOT NOISE

The compact-binary population used in the projections of the main text is generated as follows. We assume three years of observation ( $T_{\text{obs}} = 3 \text{ yr}$ ). Binary black hole (BBH) and binary neutron star (BNS) sources are drawn from a Madau–Dickinson star-formation rate [58],

$$\psi(z) \propto \frac{(1+z)^{2.7}}{1 + \left(\frac{1+z}{1+z_p}\right)^{5.6}}, \quad (\text{S49})$$

with peak redshift  $z_p = 1.9$ . The local merger rates are set to  $R_0^{\text{BBH}} = 24 \text{ Gpc}^{-3}\text{yr}^{-1}$  and  $R_0^{\text{BNS}} = 250 \text{ Gpc}^{-3}\text{yr}^{-1}$ , consistent with the GWTC-4 median values [25]. BBH primary masses follow a power law  $p(m_1) \propto m_1^{-2.35}$  with  $m_1 \in [5, 100] M_\odot$  and uniform mass ratios  $q \in [0.1, 1]$ ; BNS component masses are drawn from a Gaussian with mean  $1.33 M_\odot$  and width  $0.09 M_\odot$ , clipped to  $[1.0, 2.5] M_\odot$ . Each source is assigned a uniformly distributed sky position, a random inclination  $\cos \iota \in [-1, 1]$ , and a random polarization angle  $\psi \in [0, \pi)$ . Cosmological distances are computed assuming a flat  $\Lambda$ CDM cosmology with  $H_0 = 67.4 \text{ km s}^{-1} \text{ Mpc}^{-1}$  and  $\Omega_m = 0.3$ . The inspiral is truncated at the innermost stable circular orbit frequency  $f_{\text{ISCO}} = c^3 / (6^{3/2} \pi G M_{z,\text{tot}})$ , where  $M_{z,\text{tot}} = (m_1 + m_2)(1+z)$ .

For each event, the network signal-to-noise ratio is computed as  $\rho_{\text{net}} = \sqrt{\sum_d \rho_d^2}$ , where the per-detector SNR includes the antenna-pattern response  $F_d^+$ ,  $F_d^\times$  evaluated at the source sky position and the GPS time of the assigned segment:

$$\rho_d^2 = 4 \int_{f_{\text{min}}}^{f_{\text{ISCO}}} \frac{(F_d^{+2} h_+^2 + F_d^{\times 2} h_\times^2)}{S_n^{(d)}(f)} df, \quad (\text{S50})$$

with  $h_+^2 \propto [(1 + \cos^2 \iota)/2]^2$  and  $h_\times^2 \propto \cos^2 \iota$  encoding the inclination dependence. Events with  $\rho_{\text{net}} > 20$  are treated as individually resolved and removed from the residual population.

The time-averaged fractional energy density contributed by each residual event is

$$\Omega_\alpha^I(f) = \frac{5\pi^{5/3}}{36 H_0^2 T_{\text{obs}}} \frac{(G\mathcal{M}_z)^{5/3}}{c^3 d_L^2} f^{2/3} g_I, \quad (\text{S51})$$

where  $\mathcal{M}_z = \mathcal{M}(1+z)$  is the redshifted chirp mass,  $d_L$  is the luminosity distance, and  $g_I = (1 + \cos^2 \iota)^2 / 4 + \cos^2 \iota$  is the inclination-dependent intensity response. The corresponding circular polarization response is  $g_V = \cos \iota (1 + \cos^2 \iota)$ .

The shot-noise angular power spectra are computed from the spherical-harmonic projection of the residual events:

$$a_{\ell m}^X = \sum_\alpha \omega_\alpha^X Y_{\ell m}^*(\hat{\Omega}_\alpha), \quad C_\ell^{XY,\text{shot}} = \frac{1}{2\ell + 1} \sum_m \text{Re}[a_{\ell m}^X a_{\ell m}^{Y*}], \quad (\text{S52})$$

where the sum on  $\alpha$  runs over all residual events,  $\omega_\alpha^I = \Omega_\alpha^I(f_{\text{ref}})$  and  $\omega_\alpha^V = \Omega_\alpha^V(f_{\text{ref}})$  are the per-event amplitudes at the reference frequency, and  $\hat{\Omega}_\alpha$  is the sky position of event  $\alpha$ . For a uniform sky distribution, the shot noise is white in  $\ell$  with  $C_\ell^{XY,\text{shot}} = \sum_\alpha \omega_\alpha^X \omega_\alpha^Y / (4\pi)$ . However, foreground subtraction preferentially removes events from sky regions with stronger antenna response, breaking this uniformity and enhancing even- $\ell$  modes due to the quadrupolar antenna pattern of the detectors.

The inclination averages  $\langle g_I \rangle = 4/5$  and  $\langle g_V \rangle = 0$  (the latter by the odd symmetry of  $g_V$  under  $\cos \iota \rightarrow -\cos \iota$ ) imply that the ensemble-mean intensity-circular cross term vanishes:  $\langle g_I g_V \rangle = 0$ , since  $g_I$  is even and  $g_V$  is odd in  $\cos \iota$ . Thus the ensemble-mean shot-noise bias in  $C_\ell^{IV}$  is zero for an isotropically oriented population, although finite realizations still contribute variance. Meanwhile,  $C_\ell^{VV,\text{shot}}$  remains nonzero because the shot-noise power in each Stokes channel scales as  $\sum_\alpha (\omega_\alpha^X)^2$ . Since both  $C_\ell^{II,\text{shot}}$  and  $C_\ell^{VV,\text{shot}}$  scale in the same way with observing time, their ratio is independent of observing time and is given by

$$\frac{C_\ell^{VV,\text{shot}}}{C_\ell^{II,\text{shot}}} = \frac{\langle g_V^2 \rangle}{\langle g_I^2 \rangle} \approx 0.97. \quad (\text{S53})$$

This near-unity ratio implies that polarized shot noise is not parametrically suppressed relative to intensity shot noise, making polarization leakage a relevant systematic for intensity-only analyses.

## S-VI. POLARIZATION LEAKAGE BIAS DERIVATION

Here we derive the leakage bias  $\Delta C_\ell^{\text{pol}}$  noted in the main text. The  $I$ -only clean map  $\hat{a}_{\ell m}^I = \sum_{\ell'} (\mathcal{F}_{II})_{\ell\ell',m}^{-1} \hat{\mathcal{X}}_{\ell'm}^I$  absorbs polarization power through the dirty map. After sidereal averaging the Fisher matrix becomes diagonal in azimuthal index  $m$  (i.e.,  $\mathcal{F}_{\ell m, \ell' m'} \propto \delta_{mm'}$ ), since the Earth's rotation averages out the  $m \neq m'$  couplings. Under this  $m$ -diagonal structure, the signal content of this map is

$$\langle \hat{a}_{\ell m}^I \rangle_N = \sum_p \sum_X \sum_{\ell'} \mathcal{L}_{\ell\ell',m}^{X,(p)} \Omega_{\ell'm}^{X,p}, \quad (\text{S54})$$

where  $p \in \{s, c\}$  labels two classes of sources: the broadband ( $s$ , ‘‘shot’’) population consists of transient CBC events whose signals are short-lived compared to the observation time and span a wide frequency range, while the quasi-monochromatic ( $c$ , ‘‘continuous’’) population consists of persistent narrowband emitters such as rotating neutron stars. The index  $X \in \{I, V, +, -\}$  runs over Stokes parameters, and the leakage matrix

$$\mathcal{L}_{\ell\ell',m}^{X,(p)} = \sum_{\ell''} (\mathcal{F}_{II})_{\ell\ell'',m}^{-1} \mathcal{F}_{\ell''\ell',m}^{IX,(p)} \quad (\text{S55})$$

ouples the pipeline's  $I$ -template to the Stokes- $X$  content of population  $p$ . For the broadband population,  $\mathcal{F}^{IX,(s)}$  takes the form of Eq. (5) summed over the full frequency band. For the quasi-monochromatic population, the broadband spectral weight is replaced by a sum of narrow frequency bins centered on each source frequency. Defining the  $\Omega$ -normalized response

$$\tilde{\gamma}_{\ell m}^X(f) \equiv \frac{3H_0^2}{4\pi^2 f^3} H(f) \gamma_{\ell m}^X(f), \quad (\text{S56})$$

we write

$$\mathcal{F}_{\ell\ell',m}^{IX,(c)} = \sum_{\alpha} w_{\alpha} [\tilde{\gamma}_{\ell m}^I(f_{\alpha})]^* \tilde{\gamma}_{\ell'm}^X(f_{\alpha}), \quad (\text{S57})$$

so that each emitter samples the energy-density response at its own frequency. Because the broadband pipeline inverts the full-band  $\mathcal{F}_{II}$ , which averages the ORF structure over many frequencies, the leakage  $\mathcal{L}^{X,(c)}$  probes a fundamentally different frequency weighting and produces a distinct  $\ell$ -mixing pattern from  $\mathcal{L}^{X,(s)}$ . Moreover, since the leakage involves the inverse of  $\mathcal{F}_{II}$ , the mixing grows with  $\ell$  as the Fisher matrix becomes increasingly ill-conditioned.

Each Stokes component in a given time segment  $t$  decomposes as

$$\Omega_{\ell m}^X(t) = \bar{\Omega}_s \mathcal{A}_{\ell m}^{X,s} + \bar{\Omega}_c \mathcal{A}_{\ell m}^{X,c} + \delta\Omega_{\ell m}^{X,\text{shot}}(t), \quad (\text{S58})$$

where  $\bar{\Omega}_s$  and  $\bar{\Omega}_c$  are the intensity monopoles of the two populations,  $\mathcal{A}_{\ell m}^{X,p}$  are dimensionless fractional anisotropy fields fixed across segments (encoding large scale structure clustering for the broadband population and the persistent sky pattern for continuous emitters), and  $\delta\Omega_{\ell m}^{X,\text{shot}}(t)$  is the zero-mean shot-noise fluctuation from the finite number of transient events per segment ( $\delta\Omega_{\ell m}^{X,\text{shot}} \equiv 0$  for continuous sources). Their correlators are

$$\langle \mathcal{A}_{\ell m}^{X,p} \mathcal{A}_{\ell'm'}^{Y,q*} \rangle_S = \delta_{\ell\ell'} \delta_{mm'} \mathcal{C}_{\ell}^{XY,pq}, \quad (\text{S59})$$

$$\langle \delta\Omega_{\ell m}^{X,\text{shot}}(t) \delta\Omega_{\ell'm'}^{Y,\text{shot}*}(t') \rangle_S = \delta_{tt'} \delta_{\ell\ell'} \delta_{mm'} W_{\tau}^{XY}, \quad (\text{S60})$$

where  $\mathcal{C}_{\ell}^{XY,pq}$  is the dimensionless fractional cross-power spectrum between Stokes  $X$  of population  $p$  and Stokes  $Y$  of population  $q$ , and  $W_{\tau}^{XY}$  is the per-segment shot-noise cross-power in units of  $\Omega^2$ . The  $\delta_{tt'}$  reflects the statistical independence of shot noise across segments. Working in the spherical-harmonic basis and specializing the leakage matrix of Eq. (7) to separate broadband ( $s$ ) and continuous ( $c$ ) populations, we form  $\hat{C}_{\ell}^{II} = (2\ell+1)^{-1} \sum_m |\hat{a}_{\ell m}^I|^2$ . Substituting the above correlators, the polarization bias evaluates to

$$\Delta C_{\ell}^{\text{pol}} = \frac{1}{2\ell+1} \sum_{m,\ell'} \sum_{\substack{X,Y \\ \in \{V,+,-\}}} \left[ \mathcal{L}_{\ell\ell',m}^{X,(s)} \mathcal{L}_{\ell\ell',m}^{Y,(s)*} \left( \bar{\Omega}_s^2 \mathcal{C}_{\ell'}^{XY,ss} + \frac{W_{\tau}^{XY}}{N_{\text{seg}}} \right) + \bar{\Omega}_c^2 \mathcal{L}_{\ell\ell',m}^{X,(c)} \mathcal{L}_{\ell\ell',m}^{Y,(c)*} \mathcal{C}_{\ell'}^{XY,cc} + 2\bar{\Omega}_s \bar{\Omega}_c \text{Re} \left[ \mathcal{L}_{\ell\ell',m}^{X,(s)} \mathcal{L}_{\ell\ell',m}^{Y,(c)*} \mathcal{C}_{\ell'}^{XY,sc} \right] \right], \quad (\text{S61})$$

where  $N_{\text{seg}} = T_{\text{obs}}/\tau$ , and  $\bar{\Omega}_s, \bar{\Omega}_c$  are the intensity monopoles of the broadband and quasi-monochromatic populations, respectively.

For a single broadband population ( $c = 0$ ), Eq. (S61) reduces to

$$\Delta C_\ell^{\text{pol}} = \frac{1}{2\ell+1} \sum_{m,\ell'} \sum_{X,Y} \mathcal{L}_{\ell\ell',m}^X \mathcal{L}_{\ell\ell',m}^{Y*} M_{\ell'}^{XY}, \quad (\text{S62})$$

where  $M_{\ell'}^{XY} \equiv \bar{\Omega}_s^2 \mathcal{C}_{\ell'}^{XY,ss} + W_\tau^{XY}/N_{\text{seg}}$ . Both contributions to  $M^{XY}$  are positive semi-definite matrices in Stokes space:  $\mathcal{C}_{\ell'}^{XY,ss}$  is a covariance matrix by construction, and  $W_\tau^{XY} = \sum_\alpha \omega_\alpha^X \omega_\alpha^{Y*}$  is a Gram matrix. Their sum is therefore positive semi-definite. For each  $(m, \ell')$ , the summand takes the form  $\vec{v}^\dagger M \vec{v}$  with  $v_X = \mathcal{L}_{\ell\ell',m}^X$ , which is non-negative. Summing over all  $(m, \ell')$  preserves non-negativity, so  $\Delta C_\ell^{\text{pol}} \geq 0$ . The inequality is strict only if at least one leakage vector has nonzero projection onto the support of  $M_{\ell'}^{XY}$ .